UiT
THE ARCTIC
UNIVERSITY
OF NORWAY

Faculty of Science and Technology
Department of Physics and Technology

On Atmospheric Energy Transport by Waves

—

Tuomas Ilkka Henrikki Heiskanen

EOM-3901 Master's Thesis in Energy, Climate and Environment
December 2018

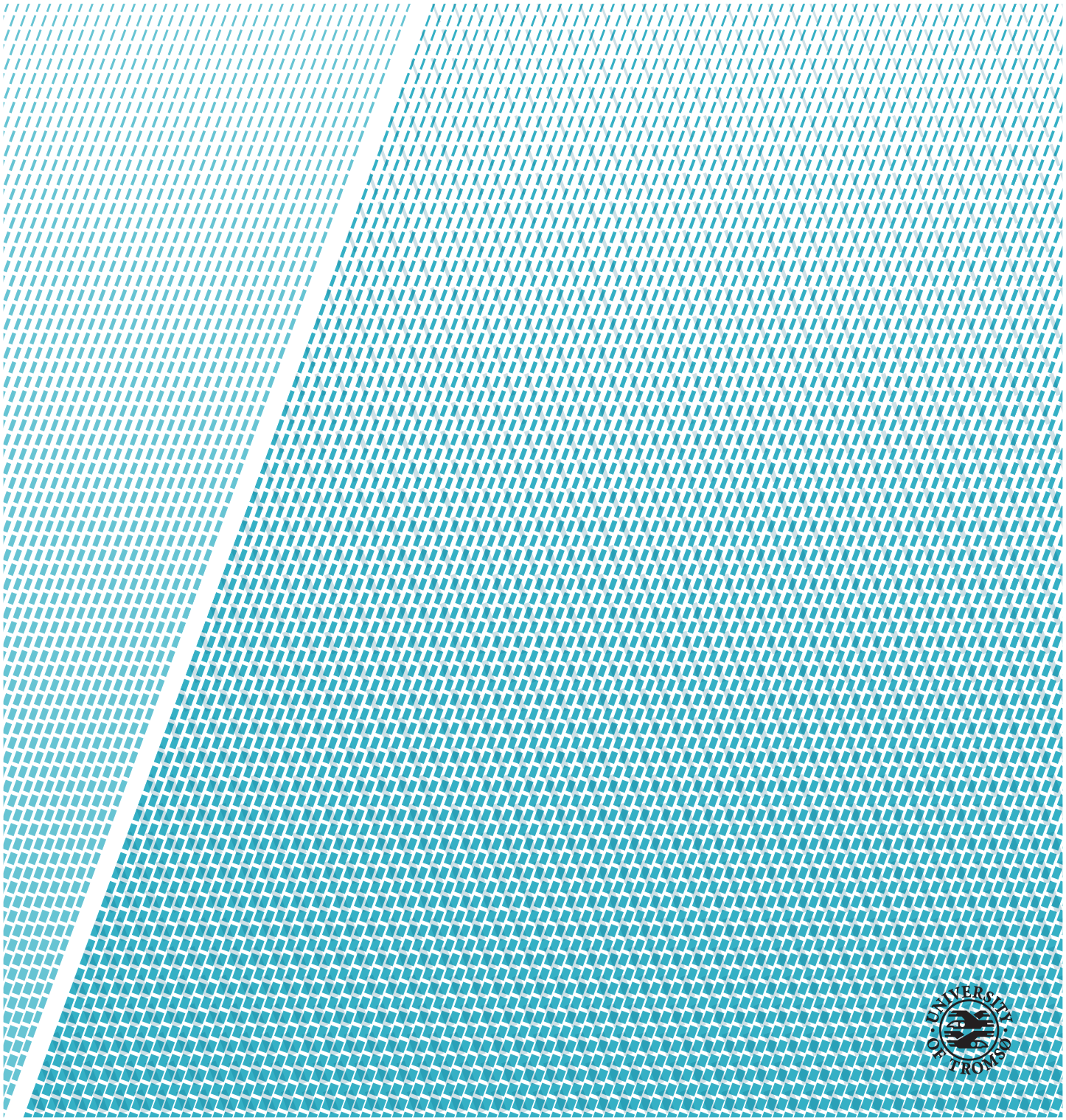

Abstract

Recently a new method, based on a Fourier decomposition in the zonal direction, for studying the atmospheric energy transport contribution by planetary and cyclone scale waves has been proposed. Recent studies based on this show that planetary waves contribute more than cyclone scale waves to the atmospheric energy transport into the Arctic. The planetary waves contribute to the Arctic amplification through latent heat transport, even when the total atmospheric energy transport is decreasing in model projections. However, the performance of the energy split method to capture transports by cyclone and planetary scale waves has not yet been evaluated. Here an attempt to evaluate the performance of the energy split method is presented. The energy split method is applied on synthetic data, where the wave structure and energy transport are known. This leads to a potential error in the energy split methods resolution of transport associated with synthetic isolated cyclones, transport is contributed to planetary waves in the Fourier spectra. When applied on atmospheric reanalysis data where only isolated cyclones are present in atmospheric state it is evident that more than 80% (70%) of the transport of dry static energy (latent heat) is contributed by planetary waves. From inspections of the vertically integrated energy transport field it is evident that the latent heat transport of cyclones is large compared to the climatology, which implies that there is a problem with the energy split method when the atmospheric state is characterized by an isolated cyclone scale wave, and that the error is especially important to consider for the latent heat transport into the Arctic. Further investigations are proposed to estimate the upper bound of the error introduced in the energy split method.

Acknowledgements

First and foremost I would like to thank all the wonderful people I have had the pleasure to get to know during my studies at UiT. From fellow students, to professors, teammates at TSI, and my roommates from "Villa Medica". You have made my years at the university a memorable time.

I would like to thank my supervisor Rune Graversen and co-supervisor Johanne Rydsaa for all the guidance and ideas during this project. It is hard imagine how this project would have ended without them.

Thanks to my family for support throughout my studies, and to my father, Ilkka, for proofreading this thesis. Last but not least my dear Karoline, who has stood by me during this project.

Contents

List of Figures

List of Tables

1

Introduction

The main energy source of the climate system is solar insolation. Annually averaged, low latitudes receive more solar insolation compared to high latitudes. This results in a temperature gradient from the equator to the poles. In general the Earth's climate system is in long-term equilibrium at each point, which implies that there has to be a poleward (meridional) energy transport to diminish the energy gradient set up by radiative imbalances between the poles and the equator. (Holton & Hakim, 2013).

Since the pre-industrial era there has been observed a global warming, which is due to anthropogenic green house gas emissions (IPCC, 2013). During the last decades an Arctic amplification has been observed, the Arctic is warming at a greater rate than the global average (Cohen et al., 2014). The enhanced temperature change is believed to be due to local feedback mechanisms such as declining sea-ice and snow cover, which reduces the surface albedo. Another feedback mechanisms affecting the Arctic temperature changes is temperature feedback: an increase in surface temperature leads to more radiation back towards space at low latitudes as compared to the Arctic. This can be attributed to a smaller increase in black body radiation per unit degree of warming at low temperatures. The effect of the temperature feedback is found, from model simulations, to be one of the main contributors to the Arctic amplification (Pithan & Mauritsen, 2014).

Most of the meridional energy transport is accomplished by the atmosphere, whilst the oceans only contribute to a minor part of the transport (Trenberth

& Caron, 2001). The atmospheric energy transport affects the temperature in the Arctic; at the Arctic boundary (~ 70°N) the atmospheric energy transport (Figure 1.1) is comparable to the incoming solar radiation received by the Arctic (Peixoto & Oort, 1992), hence changes in atmospheric energy transport may be an important feature as a contributing factor to the Arctic amplification (Graversen, 2006). This indicates that changes in the atmospheric circulation patterns might change the Arctic climate (Graversen et al., 2008). Climate models suggest that the atmospheric energy transport into the Arctic will remain constant or even decrease in the future (Hwang et al., 2011; Kay et al., 2012).

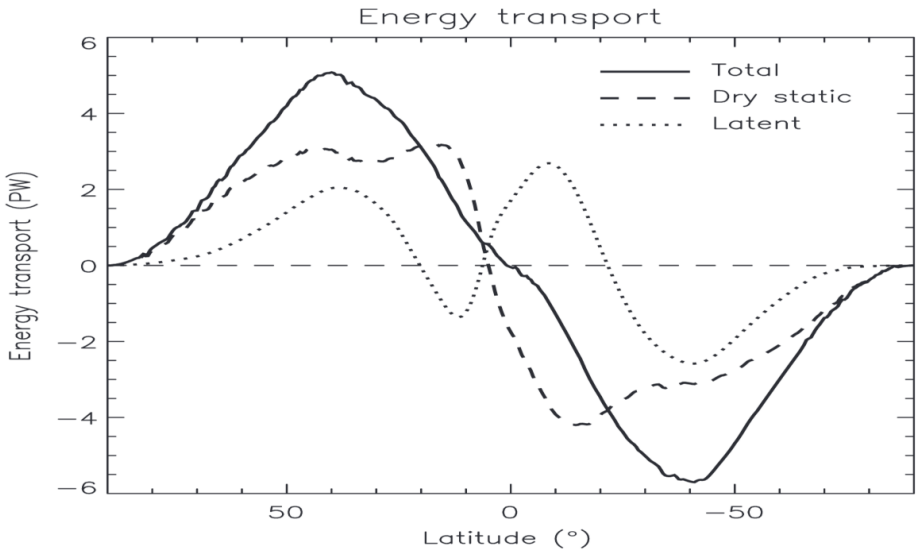

Figure 1.1: The total energy transport as a function of latitude. Computed for the years 1979 – 2012. Adapted from Graversen and Burtu (2016).

In order to examine the atmospheric transport of energy a energy split method for decomposing the atmospheric energy transport into contributions from planetary and synoptic scale waves was recently proposed by Graversen and Burtu (2016). Based on the energy split method they showed that planetary scale waves are contributing to the largest portion of the atmospheric energy transport into the Arctic (Figure 1.2). The planetary waves are shown to contribute more than the synoptic waves in both the latent heat and dry static energy transports. Based on the energy split method, they found that changes in the atmospheric circulation patterns contribute to the Arctic amplification, even if the overall energy transport remains constant or declines. This is due to the fact that the Arctic cooling due to a projected reduction of total energy transport by planetary waves will be compensated for by the warming caused by the increase in planetary latent heat transport (Graversen & Burtu, 2016).

The energy split method was developed recently, and its performance has not yet been evaluated.

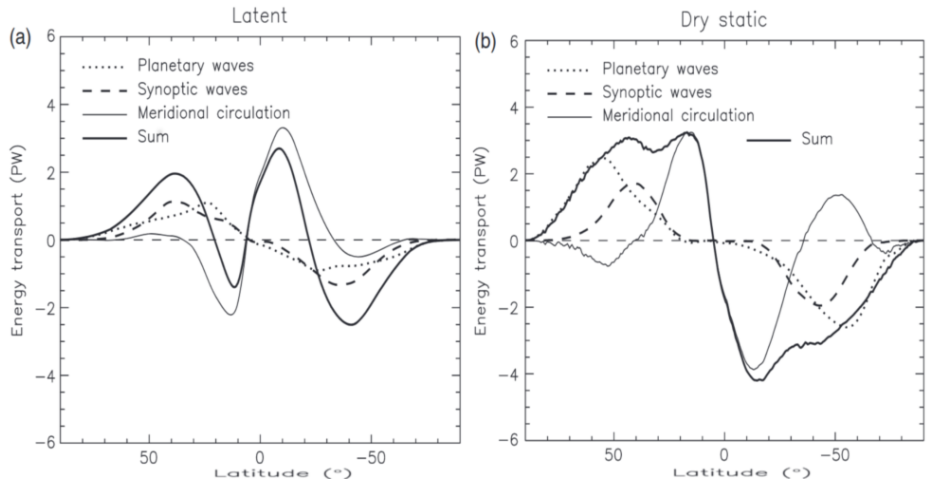

Figure 1.2: Dry static energy (b) and Latent heat (a) transport split into planetary waves, synoptic waves, and meridional circulation. Adapted from Graversen and Burtu (2016)

The objective of this study is to evaluate the performance of the energy split method based on the question: How well does the energy split method represent a split of the energy transport into planetary and synoptic (cyclone) scale waves? We try to answer this question by applying the energy split method developed by Graversen and Burtu (2016) to idealized synthetic data where the wave structure and associated energy transport are known. Additionally, we will apply the energy split method to real cases where the wave structure in the atmosphere is known.

In Chapter 2 we present the relevant theories of atmospheric circulation, meridional energy transport and spectral decompositions relevant for this study. The data and methods used in this study are presented in Chapter 3, whilst the energy split method is applied on synthetic and real cases in Chapter 4. In Chapter 5 we inspect the mean energy transport field for several cases found by applying a conditional filter on the geopotential height, and compare the energy split components with the longitude-dependent meridional transport. In Chapter 6 we summarize the study, present concluding remarks and possible future work.

2

Background Theory

2.1 General Circulation

The meridional energy transport is accounted for by the general circulation patterns in the atmosphere. The general circulation of the tropics and mid-latitudes are different in their characteristics. In the tropics, latitudes in the range 0° to ~ 23°, the meridional circulation is dominated by the Hadley circulation. The Hadley circulation is an overturning cell that is induced due to a difference in radiative heating/cooling between the tropics and the mid-latitudes. The air at the equator is heated, which induces convective motions. As the air rises it will propagate poleward, both north and south of the equator. As the air is propagating towards the poles it will cool, which will result in descending cold air in the subtropics. The cold air that descends to the surface will then propagate back towards the equator. In addition to the poleward motions in the Hadley cell the air will be deflected by the Coriolis force towards the right on the northern hemisphere and the left on the southern hemisphere. The wind patterns emerging due to the Coriolis effect are the equatorial trade winds at the surface, and the jet-stream at high altitudes (Marshal & Plumb, 2008).

In theory it is possible to have a meridional circulation pattern consisting of Hadley cells from the tropics to the poles. A circulation pattern like that is mathematically possible, and would not violate the laws of physics. But, this is not the case in the atmosphere. A zonally-symmetric hemispheric-wide Hadley circulation would be baroclinically unstable. Thus it would break down into

baroclinic eddies outside the tropics, which would alter the circulation pattern through heat and momentum fluxes (Holton & Hakim, 2013).

Hence the circulation patterns in the mid-latitudes are dominated by Rossby waves and baroclinic eddies.

2.1.1 Rossby Waves

Rossby waves are one of the most important wave types present in the climate system (Vallis, 2017). Rossby waves are large-scale waves that usually dominate the atmospheric patterns of the mid- to high-latitudes. The driving process behind Rossby waves depends on whether we have a barotropic[1] or baroclinic[2] atmosphere. In a barotropic atmosphere Rossby waves are induced due to the conservation of absolute vorticity, and exist due to the latitudinal dependence of the Coriolis parameter. Baroclinic Rossby waves on the other hand are induced by a potential vorticity conserving motion, and exist due to a gradient in the potential vorticity field.

To derive the dispersion relation for barotropic Rossby waves we start with the adiabatic shallow water[3] quasi-geostrophic potential vorticity equation;

$$\frac{\mathrm{D}q}{\mathrm{D}t} = \frac{\partial q}{\partial t} + \boldsymbol{u} \cdot \nabla q = 0, \tag{2.1}$$

where $q = q(x, y, t)$ is the potential vorticity and $\boldsymbol{u} = \boldsymbol{u}(x, y, t)$ is the horizontal velocity. From the underlying assumptions of the shallow water equations we have that the density is constant and thus $\nabla \cdot \boldsymbol{u} = 0$. Thus we can relate the velocity with a stream function, ψ, as

$$\boldsymbol{u} = (u, v, 0) = \left(-\frac{\partial \psi}{\partial y}, \frac{\partial \psi}{\partial x}, 0 \right). \tag{2.2}$$

Assuming that we look only at a single layer of fluid we can write the potential vorticity as

$$q = \zeta + f - k_d^2 \psi, \tag{2.3}$$

where $\zeta = \nabla^2 \psi$ is the relative vorticity, f is the planetary vorticity and $k_d^2 = \frac{1}{L_d^2}$, where L_d is the Rossby radius of deformation. The Rossby radius of deformation

1. A barotropic atmosphere is an atmosphere where the isoterms and isobars are aligned, the density is only a function of pressure.
2. A baroclinic atmosphere is an atmosphere where the isobars and isoterms are crossing, such that the density is a function of both temperature and pressure.
3. The shallow water equations are based on the assumptions that the depth of the fluid is small compared with the considered length scale ($H << L$), that the density within a layer is constant $\rho = \rho_0$, and that the fluid is in hydrostatic balance.

is the length scale at which rotational effects (Coriolis force) has a large enough influence to turn the velocity such that it is parallel to the isobars. In other words it is the distance waves can travel away from an initial perturbation. Linearizing Equation 2.2 and Equation 2.3 around a time-independent basic state we get

$$q = \bar{q}(y) + q'(x, y, t), \quad \psi = \bar{\psi}(y) + \psi'(x, y, t). \tag{2.4}$$

In addition to the potential vorticity, q, and the stream function, ψ, the zonal and meridional velocities are linearized. The meridional velocity is linearized around a basic state without any mean flow, whilst the zonal velocity is linearized around a basic state with mean speed $\bar{u}$. The basic states are based on the fact that in the regions we are considering the Coriolis force is strong, and thus will result in a basic state with strong eastward flow. For all the linearizations we assume that the deviations from the basic state are small compared to the basic state. Inserting q from Equation 2.4 into Equation 2.1 we get

$$0 = \frac{\partial \bar{q}}{\partial t} + \frac{\partial q'}{\partial t} + \bar{\boldsymbol{u}} \cdot \nabla \bar{q} + \bar{\boldsymbol{u}} \cdot \nabla q' + \boldsymbol{u}' \cdot \nabla \bar{q} + \boldsymbol{u}' \cdot \nabla q'. \tag{2.5}$$

We assume that the basic state of q is independent of time, i.e. $\frac{\partial \bar{q}}{\partial t} = 0$. By assuming that the basic state, $\bar{q}$, is a solution to Equation 2.1 we get that $\bar{\boldsymbol{u}} \cdot \nabla \bar{q} = 0$, since $\frac{\partial \bar{q}}{\partial t} = 0$. Since the deviations from the mean are small, products of deviations will be even smaller. Thus we can disregard the terms that are multiples of deviations. By using the linearization of the velocity, and by disregarding multiples of deviations, Equation 2.5 becomes;

$$\frac{\partial q'}{\partial t} + \bar{u}\frac{\partial q'}{\partial x} + v'\frac{\partial \bar{q}}{\partial y} = 0. \tag{2.6}$$

Since we only consider the motions for a single layer of fluid we can insert Equation 2.3 for q in Equation 2.6.

$$\frac{\partial}{\partial t}\left(\zeta' + f - k_d^2\psi'\right) + \bar{u}\frac{\partial}{\partial x}\left(\zeta' + f - k_d^2\psi'\right) + v'\frac{\partial}{\partial y}\left(\bar{\zeta} + f - k_d^2\bar{\psi}\right) = 0. \tag{2.7}$$

To further simplify the expression we restrict the motion to a β-plane such that $f = f_0 + \beta y$, where f_0 is a constant that is defined by the initially considered latitude. In addition we use the linearizations in Equation 2.4, with the exception that the basic state will only be a linear function of y due to the fact that we only consider motions in a single layer of fluid. From the relation between the velocity and the stream function we thus get that $\bar{\psi} = -\bar{u}y$. Inserting this into Equation 2.7 yields

$$0 = \left(\frac{\partial}{\partial t} + \bar{u}\frac{\partial}{\partial x}\right)\left(\nabla^2\psi' - k_d^2\psi'\right) + \left(\beta + k_d^2\bar{u}\right)\frac{\partial \psi'}{\partial x}. \tag{2.8}$$

To derive a dispersion relation for the Rossby waves we seek wave solutions, that are periodic at the boundaries in x, of Equation 2.8 on the form

$$\psi' = \tilde{\psi} e^{i(kx+ly-\omega t)}, \tag{2.9}$$

where $\tilde{\psi}$ is a time- and space-independent constant, k the zonal wavenumber, l the meridional wavenumber, and ω the frequency in time. Substituting for ψ' in Equation 2.8 from Equation 2.9 we get

$$\omega = \frac{k\left(\bar{u}\left(l^2+k^2\right)-\beta\right)}{(l^2+k^2)+k_d^2} = \bar{u}k - k\frac{\beta+\bar{u}k_d^2}{K^2+k_d^2}, \quad K^2 = k^2+l^2. \tag{2.10}$$

From the dispersion relation in Equation 2.10 we can derive expressions for the phase- and group-velocities of the Rossby waves. Assuming that we have an infinite deformation radius, such that $k_d \approx 0$, the phase velocity in the zonal direction becomes

$$c_p^x = \frac{\omega}{k} = \bar{u} - \frac{\beta}{K^2}. \tag{2.11}$$

From Equation 2.11 we see that in the absence of a mean flow $\bar{u}$ the Rossby waves will travel westward, and the long waves will travel faster than the short waves. In addition we see that we will have stationary waves for wavenumbers such that $\bar{u} = \frac{\beta}{K^2}$. The zonal group velocity is given as

$$c_g^x = \frac{\partial\omega}{\partial k} = \bar{u} + \frac{\beta\left(k^2-l^2\right)}{\left(k^2+l^2\right)^2} = c_p^x + \frac{2\beta k^2}{\left(k^2+l^2\right)^2}. \tag{2.12}$$

Equation 2.12 implies that Rossby wave packets in the zonal direction move eastward faster than their phase speed c_p^x. In addition to that we see that stationary waves will only be able to propagate eastward (Vallis, 2017). The derivations shown in this section are for a remarkably simplified case. The dispersion relation in Equation 2.10 describes the motions of barotropic Rossby waves in a fluid consisting of a single layer. For a realistic description of the motion of Rossby waves we would have to perform the same calculations in a stratified fluid, which would be a lot more complex. The simplified derivation captures some of the important properties of the Rossby waves, i.e. that they propagate westward compared to the mean flow. In addition the mechanism behind Rossby waves will essentially be the same for the more complex situations as in the simplified derivation. Consider a material line of stationary fluid parcels at a constant latitude, and let them be perturbed off the latitude such that the Coriolis parameter changes. Due to potential vorticity conservation the change in the Coriolis parameter will result in a negative relative vorticity change if the displacement is northward, or a positive change if the displacement is southward (Figure 2.1). This will result in a meandering back towards the original latitude. In the end this will result in a Rossby wave with the phase propagating westward (Vallis, 2017).

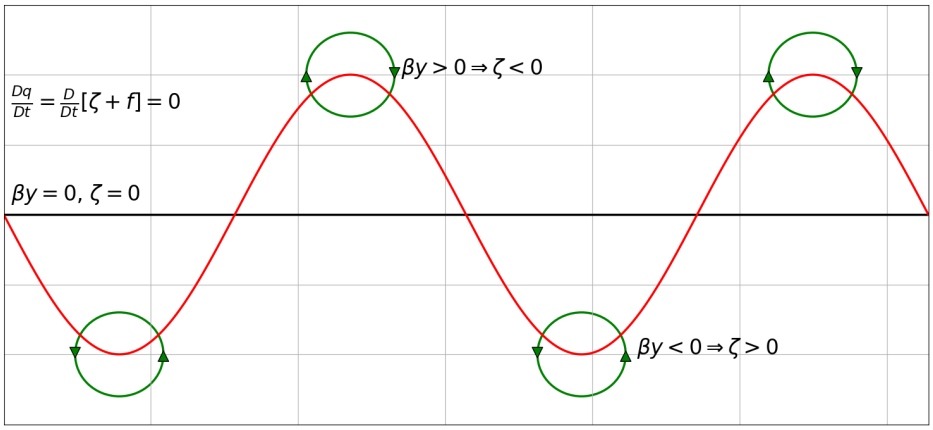

Figure 2.1: Schematic view of the mechanism of Rossby wave formation through conservation of potential vorticity. The black line is the initial latitude of the material line of fluid, and the red line represents the Rossby wave after formation. The circles describes the rotation of the fluid, with the arrows indicating the direction of rotation.

2.1.2 Cyclones

Cyclones are present both in the mid-latitude and tropical atmosphere. They exist both as warm core convective systems and cold core baroclinic systems. The warm core systems are most prominent in the tropics, whilst the baroclinic cyclones are the dominating weather patterns at the mid-latitudes. Baroclinic cyclones develop due to baroclinic instability. The isobars and isoterms of a baroclinically unstable atmosphere are tilted with height. On the northern hemisphere the isobars are tilted westward with height, and the isoterms eastward with height. By perturbing a baroclinically unstable state, we will get a transport of cold air southward to the west of the surface low, and warm air northward to the east of the surface low. The transport of cold air southward to the left of the surface low will further enhance the high level depression in the geopotential height, and thus intensify the cold air transport. This will end up producing a flow that is rotating around the center of the surface depression, a cyclone (Figure 2.2).

Baroclinic cyclone development requires strong temperature gradients. These are often found at the main polar front, and at the transition between the ocean and sea-ice. On the northern hemisphere cyclones typically develop over the ocean-basins close to the ice sheets, e.g. the Greenland ocean basin.

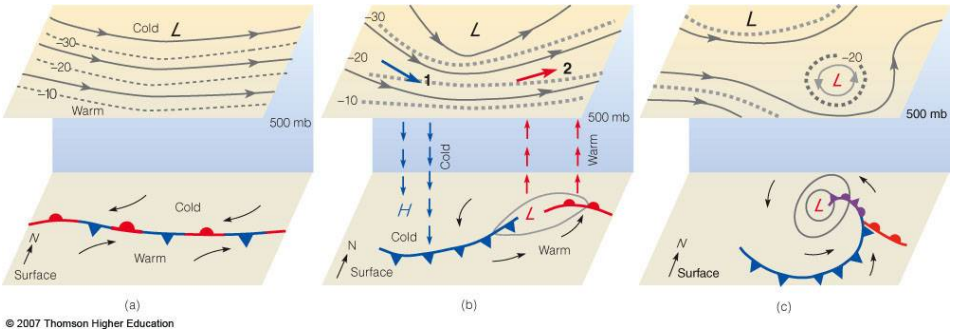

Figure 2.2: A schematic view of cyclone formation through baroclinic instability. (a) describes the initial state, (b) the perturbed state, and (c) the formed cyclone (*Warm and Cold Advection Generated by Short Waves at Mid Levels*, 2007).

2.2 Meridional Energy Transport

Due to the pole-equator energy gradient we will have a meridional energy transport present in the atmospheric circulation. Let us consider a northward flow at latitude ϕ, across an infinitesimal area dA of height dz and longitudinal width dθ, such that

$$\mathrm{d}A = R\cos(\phi)\mathrm{d}\theta\mathrm{d}z, \tag{2.13}$$

where R is the radius of the Earth, and ϕ the latitude we consider. The mass flux due to the northward flow across dA can be expressed as

$$m_f = \rho v \mathrm{d}A, \tag{2.14}$$

where ρ is the density of the air, and v the meridional component of the velocity. Thus the energy flux across dA can be expressed as

$$E_f = Em_f = E\rho v\mathrm{d}A, \tag{2.15}$$

where E is the moist static energy per unit mass. E is given as

$$E = c_pT + gz + Lq + \frac{1}{2}\boldsymbol{u}\cdot\boldsymbol{u}, \tag{2.16}$$

where c_p is the specific heat capacity of air, T the temperature of the air, g the gravitational acceleration, z the height, L the latent heat of evaporation, q the specific humidity, and $\boldsymbol{u}$ the velocity. The terms in Equation 2.16 are total energy (c_pT), potential energy (gz), latent heat (Lq), and kinetic energy ($\frac{1}{2}\boldsymbol{u}\cdot\boldsymbol{u}$). Integrating across a latitudinal wall yields the meridional transport across the latitude ϕ.

$$vE(\phi) = \int\int \rho vE\mathrm{d}A = a\cos\phi\int_0^{2\pi}\int_0^{\infty}\rho vE\mathrm{d}z\mathrm{d}\theta. \tag{2.17}$$

For the atmosphere in general it is reasonable to assume a state where the atmosphere is in hydrostatic balance. Hydrostatic balance implies that the buoyancy forces are balancing the gravity, such that

$$\rho g = -\frac{\partial p}{\partial z}. \tag{2.18}$$

Solving Equation 2.18 for ∂z and inserting into Equation 2.17 yields the following

$$vE(\phi) = \frac{a}{g}\cos\phi \int_0^{2\pi}\int_0^{p_s} vE\mathrm{d}p\mathrm{d}\theta, \tag{2.19}$$

where p_s is the surface pressure. Equation 2.19 is an expression for the meridional energy transport. This includes both dry static and latent energy. (Marshal & Plumb, 2008)

2.3 Classical Decomposition – Stationary and Transient Eddies

The classical way of decomposing the meridional energy transport is by decomposing it into the components due to meridional circulation, stationary eddies, and transient eddies. This decomposition is derived in Peixoto and Oort (1992), and the derivation that is presented here follows this closely. We derive the equations for the components for an arbitrary atmospheric field at first, and then substitute the atmospheric fields that are included in the energy transport. To derive the split we have to introduce some operators and definitions. The zonal averaging operator is defined as

$$[A] = \frac{1}{2\pi}\int_0^{2\pi} A\,\mathrm{d}\theta, \tag{2.20}$$

and the time-averaging operator is defined as

$$\overline{A} = \frac{1}{T}\int_0^{T} A\,\mathrm{d}t, \tag{2.21}$$

where A in both Equation 2.20 and Equation 2.21 is an atmospheric field, and T is the averaging period in time. In addition to the averaging operators we need to track the deviations from the averages. Thus we define the deviations from the means such that

$$A = [A] + A^*, \quad [A^*] = 0, \tag{2.22}$$

and

$$A = \overline{A} + A', \quad \overline{A'} = 0, \tag{2.23}$$

where A^* is the deviation from the zonal mean, and A' is the deviation from the time-average. When we consider the energy transport we need the product of two atmospheric fields, i.e. the velocity field and an energy field. Thus we introduce B, which has the same properties as A in Equations (2.20) – (2.23). The product AB can thus be written as

$$AB = ([A] + A^*)([B] + B^*) = [A][B] + [A]B^* + A^*[B] + A^*B^*. \tag{2.24}$$

By taking the zonal mean of Equation 2.24 we get

$$[AB] = [A][B] + [A^*B^*], \tag{2.25}$$

due to the fact that $[B^*] = [A^*] = 0$. The term $[A^*B^*]$ in Equation 2.25 is the zonal covariance of A and B. It describes how the two fields depend on each other, and will be equal to zero if the fields are independent, in the zonal direction, of each other. By applying Equation 2.23 we get that

$$A = \overline{A} + A', \quad B = \overline{B} + B' \Rightarrow [A] = \overline{[A]} + [A'], \quad [B] = \overline{[B]} + [B']. \tag{2.26}$$

Inserting Equation 2.26 into Equation 2.25 yields

$$[AB] = \overline{[A]}\,\overline{[B]} + \overline{[A]}[B'] + [A']\overline{[B]} + [A'][B'] + [A^*B^*]. \tag{2.27}$$

We are not only interested in the zonal-mean of the quantity AB, but also the time-average. Letting Equation 2.21 operate on Equation 2.27 yields

$$\overline{[AB]} = \overline{[A]}\,\overline{[B]} + \overline{[A'][B']} + \overline{[A^*B^*]}. \tag{2.28}$$

Applying the fact that $\overline{AB} = \overline{A}\,\overline{B} + \overline{A'B'}$ on the last term of Equation 2.28 yields

$$\overline{[AB]} = \overline{[A]}\,\overline{[B]} + \overline{[A'][B']} + \left[\bar{A}^*\bar{B}^*\right] + \overline{[A'^*B'^*]}, \tag{2.29}$$

which can be rewritten as

$$\overline{[AB]} = \overline{[A]}\,\overline{[B]} + \overline{[A'B']} + \left[\bar{A}^*\bar{B}^*\right], \tag{2.30}$$

by using the fact that $\overline{[A'B']} = \overline{[A']}\,\overline{[B']} + \overline{[A'^*B'^*]}$. The expression in Equation 2.30 is the one used to decompose the meridional energy transport into stationary and transient eddies. Letting $A = v$, the meridional velocity component, and $B = Lq$, the latent heat content, and inserting into Equation 2.30 yields

$$L\overline{[vq]} = L\left(\overline{[v]}\,\overline{[q]} + \overline{[v'q']} + [\bar{v}^*\bar{q}^*]\right). \tag{2.31}$$

Equation 2.31 is an expression for the split of the northward moist energy transport into contributions from the mean meridional circulation $L\overline{[v]}\,\overline{[q]}$, the transient eddies $L\overline{[v'q']}$, and the stationary eddies $L[\bar{v}^*\bar{q}^*]$. A similar split can be done for any energy field, and can thus be done for the total meridional

energy transport (Peixoto & Oort, 1992). It is important to note that the separation of transient and stationary eddies will depend on which averaging period T in Equation 2.21 is chosen. The split into meridional circulation, transient eddies and stationary eddies does not take into account the scale of the eddies, Rossby waves and cyclone scale waves can both be transient or stationary. Stationary Rossby waves are e.g. waves produced by the orography of the Rocky mountains and Himalayas on the northern hemisphere. Cyclone scale waves are usually transient, but at locations where we have strong temperature gradients cyclones can be observed as a part of the time-mean field, e.g. in the sea-basin between Greenland and Iceland. Thus the split into transient and stationary eddies can not be used to separate the transport to the contribution of waves of different length scales.

2.4 Spectral Decomposition

Spectral methods are widely applied in meteorology and atmospheric physics. From numerical weather prediction to spectral analysis across latitude circles. Spectral methods are also applied in the time-domain, and can be used to identify periodic patterns in the climate system. In the time-frequency spectral decomposition we transform from the time-domain to the frequency-domain by performing a decomposition of the field into a Fourier series. A similar decomposition can be made in the zonal direction, where we transform from the longitude domain to the wavenumber domain (Peixoto & Oort, 1992).

The Fourier series is a common spectral representation of a periodic field. Due to its mathematical simplicity it is easily applicable to all kinds of problems, and is thus widely used in technology and physics applications. We define the Fourier series representation of a field $f(x)$, and the Fourier components a_n and b_n as;

$$f(x) \sim \frac{a_0}{2} + \sum_{n=1}^{\infty} \left[a_n \cos\left(\frac{2\pi x}{L}\right) + b_n \sin\left(\frac{2\pi x}{L}\right) \right], \tag{2.32}$$

$$a_n = \frac{2}{L} \int_0^L f \cos\left(\frac{2\pi x}{L}\right), \quad n = 0, 1, 2, 3, \ldots,$$

$$b_n = \frac{2}{L} \int_0^L f \sin\left(\frac{2\pi x}{L}\right), \quad n = 1, 2, 3, \ldots,$$

where n is the wavenumber. The constraint we have on the field f is that it has to be periodic on the domain $[0, L]$. An aperiodic signal can not be represented well by a Fourier series. This is due to the fact that both the cosine and sine Fourier basis fields are periodic on the domain $[0, L]$.

2.4.1 Known Limitations

Spectral analysis has been studied for a long time, and many of its fallacies have been uncovered. The meteorological fields of interest (e.g. temperature, pressure, humidity) are usually only known at discrete locations in space and time. The sampling rate of the field, in time, determines how well we can represent the field in the spectral (frequency/wavenumber) domain. This is described by the Nyquist sampling theorem. The Nyquist theorem states that no information of a signal is lost if the sampling interval is smaller than the maximum frequency/wavenumber present in the field. In space this is expressed as in Equation 2.33

$$\text{If } \Delta x < \frac{1}{2n_{max}} \text{ then no information is lost.} \tag{2.33}$$

Another way of expressing the Nyquist sampling theorem is that the maximum frequency/wavenumber that can be resolved by the Fourier transform is given as

$$n_N = \frac{1}{2\Delta x}. \tag{2.34}$$

Equation 2.34 limits the maximum wavenumber we can resolve with a sampling interval Δx. By reducing the sampling interval we can represent phenomena with higher wavenumbers. If this condition is not met there will be an aliasing of high wavenumbers onto the low wavenumbers, which distorts the spectrum. This phenomena is called aliasing, where wavenumbers above the Nyquist frequency are interpreted as low wavenumbers. This problem is known as the sampling problem, as it is directly related to the sampling interval of the dataset. In addition to the sampling problem one has to be aware of the truncation problem. If a time series is truncated we can get ringing effects due to the discontinuities arising from the truncation. The ringing effects can be reduced by using smoothing windows in combination with the transform(Smith, 2007). But, for the latitude-wavenumber transformations this will not be necessary since the fields are periodic along one latitude circle, as long as the orography is not generating discontinuities (Peixoto & Oort, 1992).

For spectral analysis the power spectrum is a widely used, and powerful tool. The power spectrum is a measure of each of the wavenumbers n in the original field f. The power of wavenumber n of a field f is defined as

$$P_{xx}(n) = a_n^2 + b_n^2, \tag{2.35}$$

where a_n and b_n are the Fourier coefficients corresponding to wavenumber n (Smith, 2007). The power spectrum is used to determine how strong the power of a wavenumber n is in the field f.

3

Data and Methods

3.1 ERA-Interim

In this project we use the ERA-Interim reanalysis data set. ERA-Interim is a global reanalysis data set, developed by the European Centre for Medium-Range Weather Forecasts (ECMWF). The dataset extends from January 1979 to the present, and is continuously updated. ERA-Interim is based on the ECMWF Integrated Forecasting System (IFS), which is numerical model and data assimilation scheme. The reanalysis is produced using a sequential data assimilation scheme, advancing in time at 12-hourly analysis cycles. In each cycle available observations, i.e. satellite data, radio sonde data, local observations, and many more, are combined with information from a forecast model (IFS) to estimate the evolving state of the atmosphere. In each 12-hourly analysis cycle a 4D-variational analysis of the upper-air atmosphere is executed. The 4D-Var is the core components of the ERA-Interim reanalysis. ERA-Interim consists of 60-layers in the vertical, and a horizontal resolution of approximately 79 km (Dee et al., 2011). The horizontal resolution of the model is high enough to capture the phenomena we are interested in, without introducing aliasing phenomena due to under sampling when performing a spectral analysis. Additionally the upper-atmosphere fields are produced at a 6-hourly interval, which is short enough to represent the phenomena of interest. The ERA-Interim data set is used to compute the energy transport, and decompose it into waves. In addition to this we will use the 850 hPa geopotential field as an indicator of the wave patterns present in the atmosphere. The 850 hPa geopotential height field is produced as a 6-hourly field on a $0.5^\circ \times 0.5^\circ$ grid. The 850

hPa geopotential height is chosen as the field to be inspected since it is not affected by the problems arising in the resolution of the boundary layer, but is still capturing the characteristics of the atmospheric state. We inspect the atmospheric fields in the time period 1979 – 2012. This is the same time period that is considered in Graversen and Burtu (2016), and thus we use the same energy transport data as in Graversen and Burtu (2016).

3.2 Conditional Filter

To find situations where the energy split method might break down we search through the data set for isolated cyclones at specific latitudes. We are specifically interested in the isolated cyclones as they are hard to resolve with Fourier series (discussed in Section 4.3). There exists a huge range of different methods for cyclone filtering (Donohoe & Battisti, 2009; Anderson et al., 2003). Many of the applied filters are based on either a spherical harmonics decomposition or a Fourier decomposition in some manner. The method we apply is not using any sinusoids as a criterion for cyclone filtering. The reason for this choice is to keep the filter independent of the Fourier approach applied in the energy split method.

We are not only going through the dataset to find cyclones at a specific latitude, we also want the planetary wave activity to be constrained. Thus we define two thresholds used in the filter, C and T. The cyclone threshold, C, is used to specify how big the depression in the geopotential height is compared to the mean of the rest of the field. With the rest of the field we mean the field that remains after the cyclone has been removed. The number of grid data points around the cyclone center removed depends on the considered latitude, e.g. at 70° north we remove 50 points at both sides of the cyclone center, which corresponds to approximately 951 kilometers at both sides (a total of approximately 1902 kilometers are removed). The second threshold, T, is used to limit the deviations from the mean of the remaining field after we have removed the cyclone area. The example in Figure 3.1 shows a situation where the conditional cyclone filter will indicate that we have an atmospheric state at the given latitude with one cyclone, and no large-scale waves. The filter will select only situations where the minimum of the 850 hPa geopotential field is further from the mean than C, and the field outside the cyclone region is closer to the mean than T. The conditional filter is applied to fields that are rotated such that the minimum in 850 hPa geopotential height is centered in the middle of the domain. This is done both to simplify the computations performed when applying the filter, and used as the way to present the fields in a uniform way.

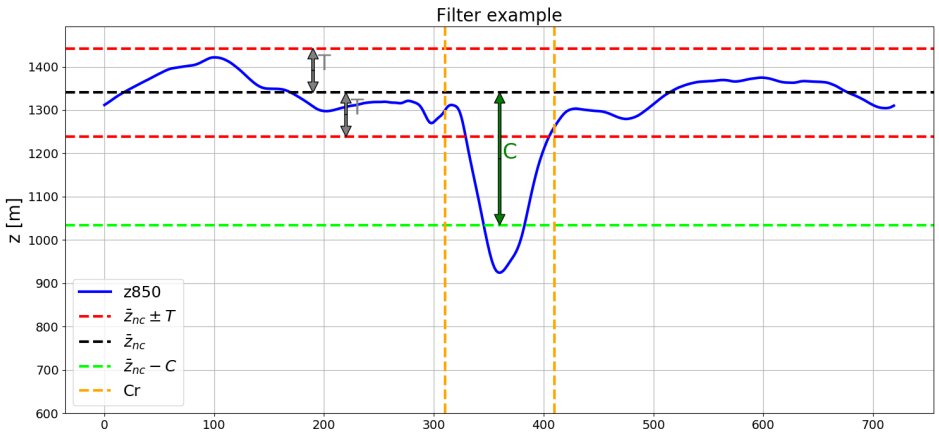

Figure 3.1: Illustrative example of the conditional filter. $\bar{z}_{nc}$ is the mean of the 850 hPa geopotential disregarding the cyclone region, Cr is indicating the cyclone region, T is the variability threshold of the cyclone free region, and C is the cyclone threshold.

3.3 Wave Decomposition

In Chapter 2 we defined the meridional energy transport, Equation 2.19. The energy transport can be further split in to the dry static and latent components. The dry static energy transport is given as

$$vD_s(\phi) = \oint \int_0^{p_s} v \left(\frac{1}{2} \boldsymbol{v} \cdot \boldsymbol{v} + c_p T + gz \right) \frac{\mathrm{d}\, p}{g} \, \mathrm{d}\, x, \tag{3.1}$$

where $\boldsymbol{v}$ is the velocity at latitude ϕ, T the temperature, c_p the specific heat capacity of air, and z the height. The latent heat-transport is given as

$$vD_L(\phi) = \oint \int_0^{p_s} v\, Lq \frac{\mathrm{d}\, p}{g} \, \mathrm{d}\, x, \tag{3.2}$$

where L is the specific heat of evaporation for water, v the meridional velocity, and q the specific humidity.

The method for decomposing the energy transport in Equation 3.1 and Equation 3.2 relies on a Fourier series expansion of v and E. To apply a Fourier series expansion we need the fields to be periodic. This will be the case for the v- and E-fields since we will look at only one latitude at a time, and that these are periodic in the longitude direction. The Fourier series of an arbitrary periodic function, with period L, is defined in Equation 2.32. The length of the integration path, L, will depend on the latitude. Such that $L = L(\phi) = 2\pi R \cos(\phi)$, where R is the radius of the Earth and ϕ the latitude. The Fourier series expansions

of v and E are thus given as

$$v(x,\phi) = \frac{a_0^v}{2} + \sum_{n=0}^{\infty} a_n^v \cos\left(\frac{n\,2\pi\,x}{L(\phi)}\right) + b_n^v \sin\left(\frac{n\,2\pi\,x}{L(\phi)}\right), \tag{3.3}$$

$$E(x,\phi) = \frac{a_0^E}{2} + \sum_{n=0}^{\infty} a_n^E \cos\left(\frac{n\,2\pi\,x}{L(\phi)}\right) + b_n^E \sin\left(\frac{n\,2\pi\,x}{L(\phi)}\right). \tag{3.4}$$

By inserting Equation 3.3 and Equation 3.4 into Equation 3.1 we get that the dry static energy transport can be written as

$$\begin{aligned} vD_s(\phi) = \oint \int_0^{p_s} &\left(\frac{a_0^v}{2} + \sum_{n=0}^{\infty} a_n^v \cos\left(\frac{n\,2\,\pi\,x}{L(\phi)}\right) + b_n^v \sin\left(\frac{n\,2\,\pi\,x}{L(\phi)}\right)\right), \\ &\left(\frac{a_0^E}{2} + \sum_{n=0}^{\infty} a_n^E \cos\left(\frac{n\,2\,\pi\,x}{L(\phi)}\right) + b_n^E \sin\left(\frac{n\,2\,\pi\,x}{L(\phi)}\right)\right) \frac{\mathrm{d}\,p}{g}\,\mathrm{d}\,x. \end{aligned} \tag{3.5}$$

By performing the multiplication of the Fourier series in Equation 3.5 we get infinitely many terms, where many of them will be cross terms,
e.g. the term $a_1 \cos\left(\frac{2\pi x}{L(\phi)}\right) a_2 \cos\left(\frac{4\pi x}{L(\phi)}\right)$. Integrating over latitude eliminates these cross terms. This is due to the fact that

$$\int_0^L \cos\left(\frac{n\,2\pi\,x}{L}\right) \cos\left(\frac{m\,2\pi\,x}{L}\right) = 0, \quad n \neq m,$$
$$\int_0^L \sin\left(\frac{n\,2\pi\,x}{L}\right) \sin\left(\frac{m\,2\pi\,x}{L}\right) = 0, \quad n \neq m,$$

and

$$\int_0^L \cos\left(\frac{n\,2\pi\,x}{L}\right) \cos\left(\frac{m\,2\pi\,x}{L}\right) = \frac{L}{2}, \quad n = m,$$
$$\int_0^L \sin\left(\frac{n\,2\pi\,x}{L}\right) \sin\left(\frac{m\,2\pi\,x}{L}\right) = \frac{L}{2}, \quad n = m.$$

Which gives us that the zonal mean of the energy transport can be written as

$$vD(\phi) = L \int_0^{p_s} \left[\frac{1}{4} a_0^v a_0^E + \sum_{n=1}^{\infty} \frac{1}{2}\left(a_n^v a_n^E + b_n^v b_n^E\right)\right] \frac{\mathrm{d}\,p}{g}. \tag{3.6}$$

The split into meridional circulation, planetary waves, and synoptic waves is done by splitting the total in Equation 3.6 into separate parts based on the wavenumber n. The split, as done in Graversen and Burtu (2016), is given as

follows

$$vE(\phi)_m = L \int_0^{p_s} \frac{1}{4} a_0^v a_0^E \frac{\mathrm{d}\,p}{g}, \tag{3.7}$$

$$vE(\phi)_p = L \sum_{n=1}^{5} \int_0^{p_s} \frac{1}{2} \left(a_n^v a_n^E + b_n^v b_n^E \right) \frac{\mathrm{d}\,p}{g}, \tag{3.8}$$

$$vE(\phi)_s = L \sum_{n=6}^{20} \int_0^{p_s} \frac{1}{2} \left(a_n^v a_n^E + b_n^v b_n^E \right) \frac{\mathrm{d}\,p}{g}. \tag{3.9}$$

The exact wavenumber (n) at which the split between planetary and synoptic phenomena is not rigid. The exact separation between planetary and synoptic scale phenomena will affect the expressions in Equations 3.8 and 3.9, but it could have been chosen differently without affecting the results of Graversen and Burtu (2016) significantly. In practice the energy split is performed by Fourier expanding $v\frac{dp}{g}$ instead of v. This yields the following expressions for the transport due to meridional circulation, planetary waves and synoptic waves respectively;

$$vE(\phi)_m = \frac{L}{4} \sum_{k=0}^{K} a_0^v a_0^E, \tag{3.10}$$

$$vE(\phi)_p = \frac{L}{2} \sum_{n=1}^{5} \sum_{k=0}^{K} \left(a_{n,k}^v a_{n,k}^E + b_{n,k}^v b_{n,k}^E \right), \tag{3.11}$$

$$vE(\phi) = \frac{L}{2} \sum_{n=6}^{20} \sum_{k=0}^{K} \left(a_{n,k}^v a_{n,k}^E + b_{n,k}^v b_{n,k}^E \right), \tag{3.12}$$

where K is the number of vertical levels in the data set, and $a_n^v,\ b_n^v$ the Fourier components of $v\frac{dp}{g}$ (Graversen & Burtu, 2016).

3.4 Monte Carlo Simulation

The statistical significance of transport fields is tested through a Monte Carlo simulation. This is a robust method which does not require any underlying assumptions of the distribution of the population. The Monte Carlo simulation is based on picking a large amount of random samples from the data, and comparing these with the fields of interest. We say that the field tested is statistically significant on e.g. a 95%-level if the hypothesis is correct for over 95% of the simulation runs.

4

Applications of the Energy Split Method

4.1 Case Studies – ERA-Interim

The first attempt at testing the performance of the energy split method (ESM) will be to inspect a few specific cases found in the ERA-Interim reanalysis data. The cases are picked by finding anomalies in the planetary and synoptic wave transports. In all the cases considered we neglect the contribution of wave 0. The reason for this is that the wave 0 component will not be accurate when we look only at one 6-hourly time step at a time. The reason for this inaccuracy is the fact that we can have a net mass-flux at short time spans in the atmosphere, the atmosphere might move a little north or south. But at large temporal scales this variation will vanish, which results in a correct representation of transport due to the wave 0 component (meridional circulation) if we average over multiple time-steps in the data set.

Case 1

In the first case we look at an atmospheric state where we have multiple synoptic phenomena located on the northern hemisphere. From Figure 4.1 we see that the geopotential at 50° north resembles an atmospheric wave 7, which is in the synoptic range. In addition we see that there is no obvious wave pattern in the

planetary range (Figure 4.1). In this specific case we observe that the transport decomposition seems reasonable. The largest portion of the transport is in the synoptic range, whilst the planetary portion of the transport is significantly smaller. The power spectrum of the geopotential at 50° north reveals that

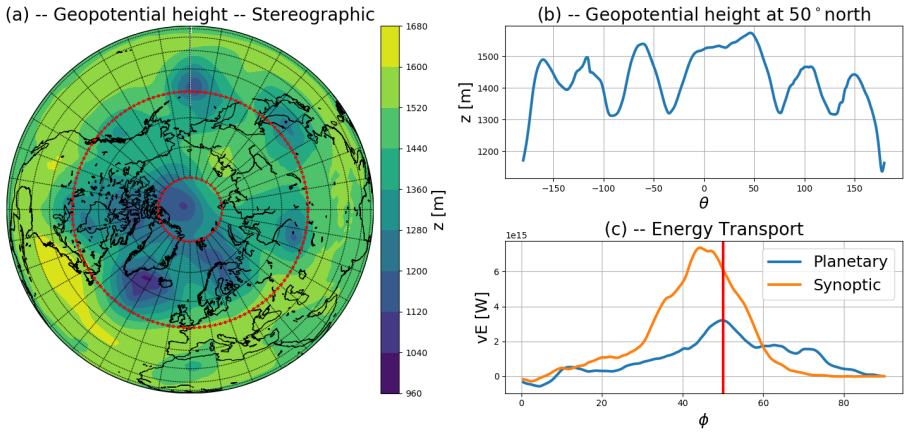

Figure 4.1: Case 1 of the case studies. The stereographic plot shows the 850hPa geopotential height on the northern hemisphere, with the red dashed line marking 50° north. The upper right plot is the 850hPa geopotential height at 50° north. The lower right plot shows the energy transport for all latitudes, split into planetary and synoptic waves. The red line in the lower right plot marks the transport at 50° north.

there is most power in wavenumber 7 (Figure 4.2). It is however evident that there is also power at lower wavenumbers, corresponding to planetary waves as well. From Figure 4.2 we observe that the largest transport component is corresponding to wavenumber 7, i.e. synoptic transport. From the power spectrum in Figure 4.2 (b) we observe that there are not only synoptic waves present, the power of wave 1 is also strong. The transport contribution of wave 1, although its strong presence in the geopotential, is weak. This is due to a phase shift between E and v, such that the Fourier coefficients of wave 1 interfere and produce only a weak transport. For this specific case the ESM seems to work well; not only are the transport fractions split in a reasonable way between synoptic and planetary transport, i.e. the synoptic waves are dominating the transport in an atmospheric state where they are the most prominent structure, but the transport peaks at the same wavenumber as the power spectrum. Which means that the transport is resolved in a sensible way.

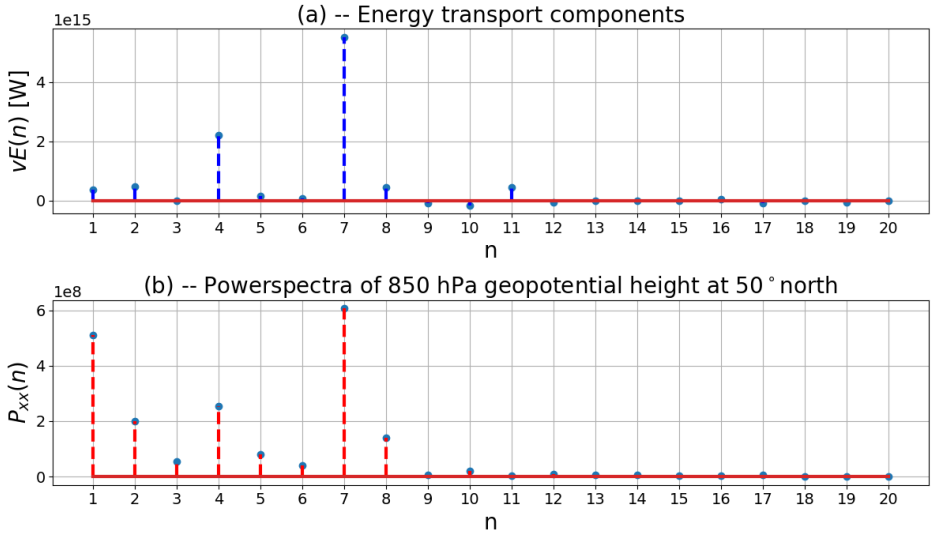

Figure 4.2: Case 1: (a) – The energy transport components at 50°north. (b) – The power spectrum of 850hPa geopotential height at 50°north.

Case 2

In the second case we inspect an atmospheric state where we have a wave pattern in the planetary range. Based on the geopotential height it is evident that there is a planetary wave 1 present in the atmosphere. The plot of the 850hPa geopotential at 60° north in Figure 4.3 illustrates the presence of the planetary wave. From the energy split we see that the planetary waves are responsible for the main part of the transport in case 2. This complies well with what we would expect, as the main atmospheric feature in the geopotential height is a planetary wave 1. From the power spectrum of the geopotential height (Figure 4.4 (b)) it becomes even clearer that there is only planetary waves present. The power spectrum is dominated by wavenumber 1 and also the rest of the wavenumbers are in the planetary range. The transport components also have a maximum at wavenumber 1, which further enhances our confidence in the ESM. In this case the ESM is producing the result we would expect by inspecting the 850hPa geopotential height field.

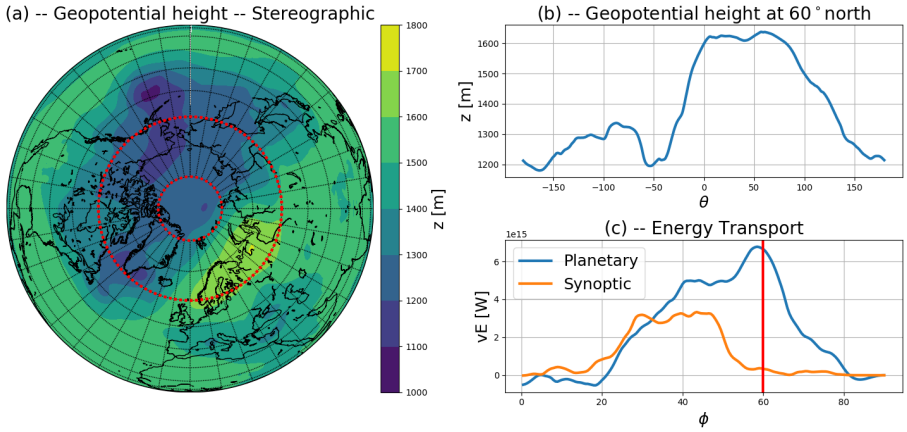

Figure 4.3: As Figure 4.1 but for case 2 of the case studies, with the red lines marking 60° north.

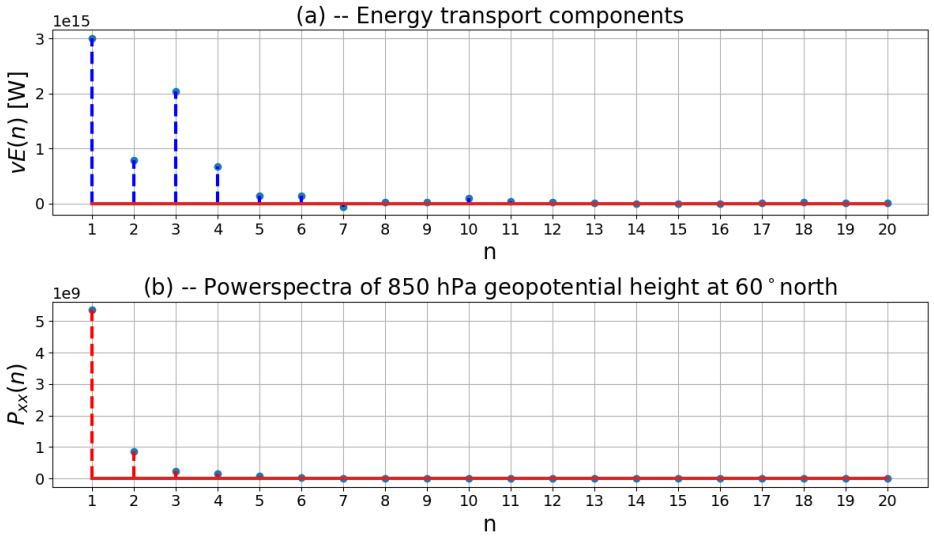

Figure 4.4: Case 2: (a) – The energy transport components at 60°north. (b) – The power spectrum of 850hPa geopotential height at 60°north.

Case 3

In the third, and last, case we look at an atmospheric state where we have no evident planetary pattern at 56° north. But, we do have a single depression in the geopotential height field that could correspond to a cyclone (plotted in the upper right plot of Figure 4.5), which is a phenomenon on the synoptic scale. The fact that the energy transport in this case is dominated by the planetary waves indicates a possible problem with the ESM; some of the energy of isolated

synoptic events might propagate to the low wavenumbers.

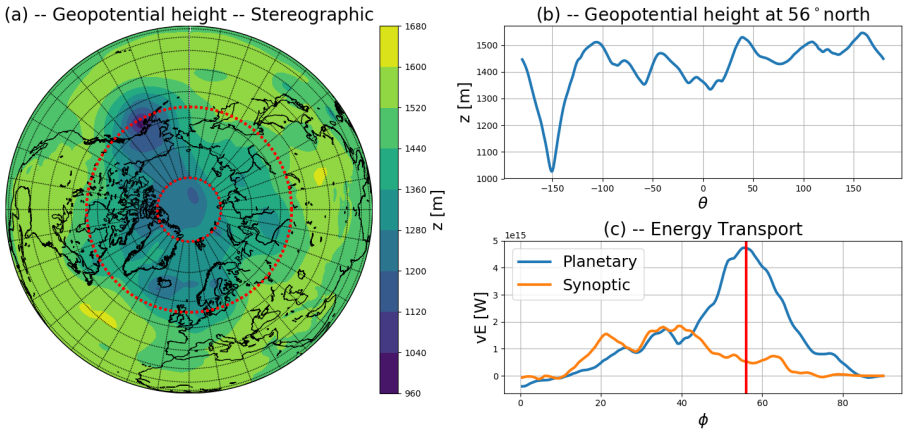

Figure 4.5: As Figure 4.1 but for case 3 of the case studies, with the red lines marking 56° north.

From the power spectrum of the 850hPa geopotential height field, in Figure 4.6 (b), we see that most of the power is located at the low wavenumbers. We can also observe, from Figure 4.6 (a), that the transport components have the maximum in the planetary scale. This shows how the power of synoptic phenomena can be propagated to the low wavenumbers. In case 3 there might also be planetary waves present, but the low peak is the dominating shape of the 850hPa geopotential height.

Such case studies can give us some insight to the strengths and weaknesses of the ESM. But, the case studies alone can not give us enough insight to draw conclusions on whether or not the ESM has major flaws. From the case studies we have observed that a possible problem seems to arise when we have an atmospheric state characterized by peaks in the fields. Thus more insight can be acquired by looking specifically into cases with negative-anomaly peaks.

4.2 Shape of Actual Cyclones Across a Latitude Cross Section

Before creating a mathematical model for a cyclone across one latitude we inspect the shape of the cross section of real cyclones at one latitude. For this the ERA-Interim reanalysis dataset has been used. The dataset is searched through for cases where we have a single cyclone at 70° north. This is done

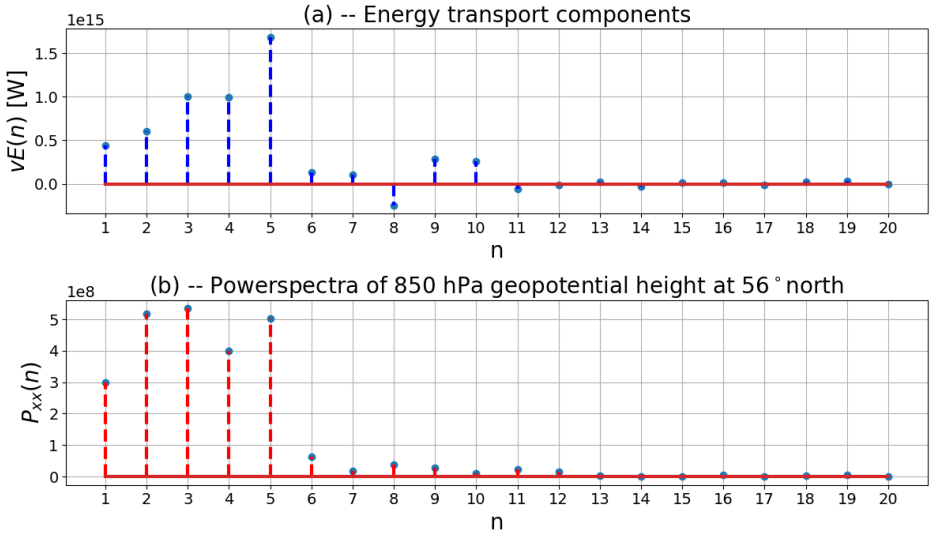

Figure 4.6: Case 3: (a) – The energy transport components at 56°north. (b) – The power spectrum of 850hPa geopotential height at 56°north.

by running the 850hPa geopotential height field through the conditional filter described in Chapter 3 (Figure 3.1). The filtering is performed for multiple thresholds C and T (which will be used in the latter chapters). First we will use the fields produced for $C \approx 275$m and $T \approx 102$m, which gives us 37 time points flagged as Rossby wave free cyclones by the filter, i.e. atmospheric states characterized by single isolated depressions in the pressure field and small variations outside the depression. Sensitivity to values of C and T is further investigated in Chapter 5.

We try to find a mathematical functions which behaves like the geopotential height field when we only have a cyclone present, and no Rossby waves. One possibility would be a Fourier series representation of the geopotential height field. But, this would not be useful in the evaluation of the ESM since the ESM itself is based on a Fourier series. A function that behaves like what we expect of the geopotential height of a single cyclone is a Gaussian, as explained in Section 4.3. Thus we use a non-linear least squares fit to fit a Gaussian

$$\hat{z} = ae^{-b(x-c)^2}, \tag{4.1}$$

to the data found by applying the conditional filter (Figure 3.1). The fit of the Gaussian in Equation 4.1 is done by estimating the parameters a, b, and c with the Levenberg-Marquardt algorithm (Sauer, 2012). The Levenberg-Marquardt algorithm requires an initial guess for the parameters to work optimally. To unify the initial guess for each case the geopotential height field is rotated such that the minimum of the field is in the middle of the domain. The resulting

function is shown in Figure 4.7. The confidence interval in Figure 4.7 is based

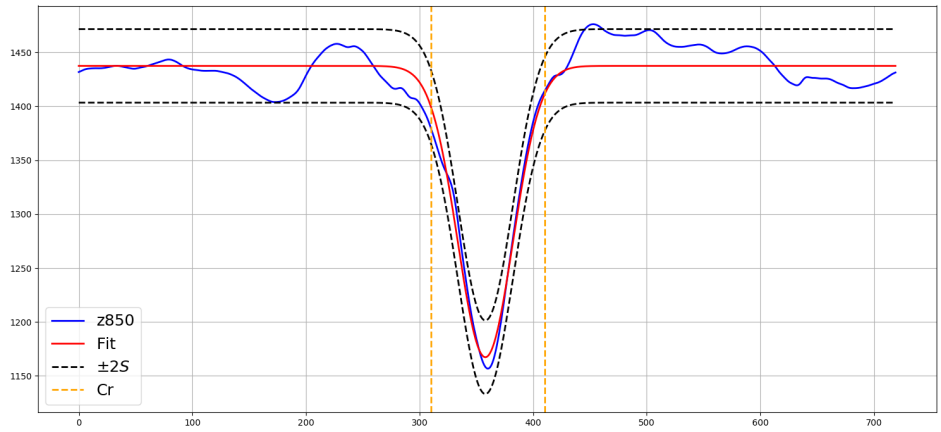

Figure 4.7: A Gaussian fitted to the 850 hPa geopotential height for one out of the 37 cases found for $T = 102$m and $C = 275$m. C_r marks the cyclone region, $\pm 2S$ the 95%-confidence interval based on the standard error of regression, z850 the 850hPa geopotential height (blue line), and the red line is the non linear least squares fit.

on the standard error of regression, which is defined as

$$S = \sqrt{\frac{\sum_{i=0}^{N} (z_i - \hat{z}_i)^2}{N}}, \tag{4.2}$$

where z_i is the data at point i, $\hat{z}_i$ is the fitted model at point i and N is the total number of points. The standard error, S, for the fitted model is $S \approx 17.04$m. From Figure 4.7 we see that the fitted Gaussian is a good fit inside the cyclone region since all the data points are contained within $\pm 2S$ of the fit. Outside the cyclone region the Gaussian does not fit the data as well as within, but it is not a bad fit outside of the cyclone region. In Figure 4.7 we only consider one case, out of the 37 found by performing our filtering.

To test the validity of the Gaussian as an artificial model of a single isolated cyclone we fit the Gaussian to each of the 37 cases and consider the mean of the fits. We are not only considering the mean of all fits, but also the Gaussian produced by taking the mean of the fitted parameters of each fit. From Figure 4.8 we see that the mean fit and the mean parameter fit are almost the same, only differing a little in the steepness of the curve. By inspection, and from the fact that the standard error of regression $S \approx 38.6$m is small compared to the mean fields, we can conclude that the Gaussian can be used as an idealization of the geopotential height field cross section of an actual cyclone across a latitude circle. It is important to note that the Gaussian (Equation 4.1) does not capture fluctuations outside the cyclone region well, but we do not

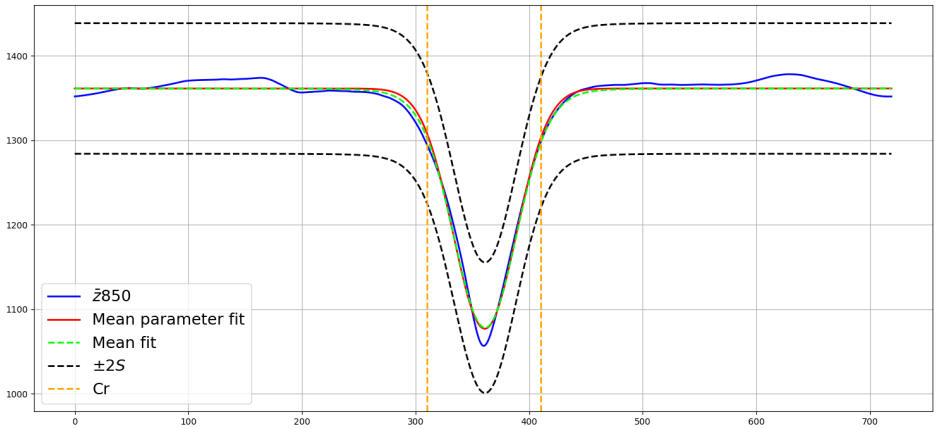

Figure 4.8: Plot of the mean 850hPa geopotential height, where each field has been centered such that the cyclones are in the middle of the domain, the mean of the fits to each of the field (green line), and the Gaussian produced by taking the mean of the parameters of each of the 37 fits (red line).

attempt to make a model for these fluctuations. The Gaussian works as an idealization of dominant patterns in the geopotential height field when we have an isolated cyclone as the main feature of the field.

4.3 Artificial Cyclones in a Synthetic Atmosphere

The mathematics of the ESM split are not very complex. The split is based on a simple Fourier series expansion, and truncation of the resulting infinite series. So, what are the possible sources of error for the energy split? By truncating the series we will not get a complete representation of the original signal. This effect should not be very large, as we can choose how many terms we want to include. The more terms we include, the smaller the error will be. A more significant source of error will be whether or not the wavenumbers in the Fourier series correspond to the actual atmospheric phenomena. In other words, does a wave 1 in the Fourier transform correspond to the presence of an atmospheric wave 1?

4.3.1 Idealized Cases

The waves observed in the atmosphere will rarely be pure shaped waveforms, consisting of only one sinusoidal component. To illustrate some of the possible problems of the ESM we can inspect the power spectra of some pure waveforms. The first waveform we inspect is a superposition of a wave 1, 3, and 6. This can

be expressed mathematically as

$$f(x) = \cos(2\pi x) + \cos(6\pi x) + \cos(12\pi x). \tag{4.3}$$

The waveform in Equation 4.3 and its power spectrum are shown Figure 4.9.

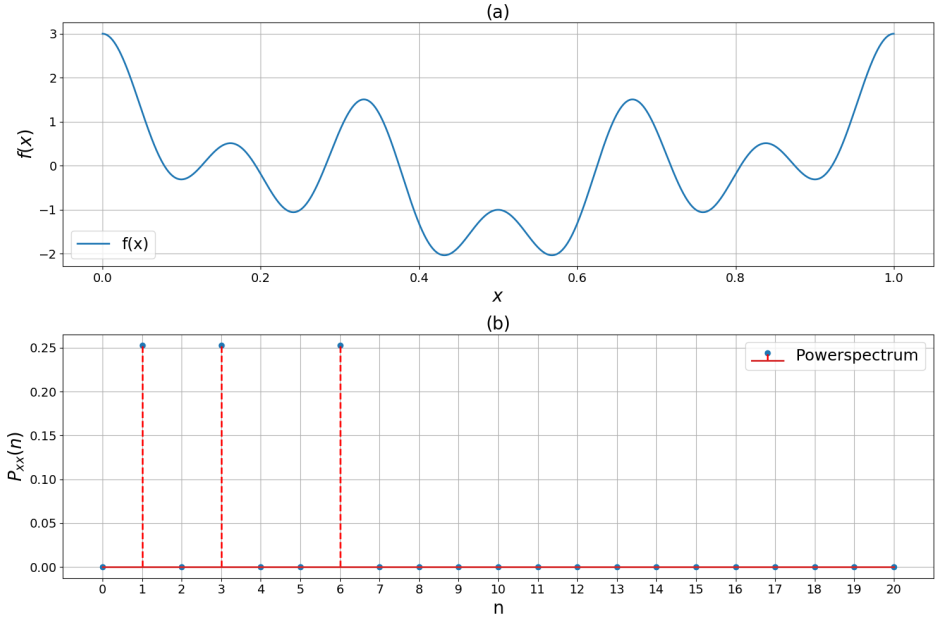

Figure 4.9: (a) - Plot of the waveform in Equation 4.3 and (b) - The power spectrum of the waveform in Equation 4.3.

From Figure 4.9 we see that the Fourier transform resolves the waveform completely. This is due to the fact that each of the represented frequencies are completely represented by one single Fourier basis function each. Thus, in cases where the fields are composed of pure sinusoids, with integer wavenumbers, the ESM will work without problems. This will not ever be the case for the atmosphere, where local perturbations will result in spikes which are not completely resolved by sinusoids. In some cases we might have isolated cyclones, which does not show any global pattern, e.g. case 3 of the previous section. These are shown in the pressure fields as single depressions, without any other strong patterns present; the pressure field of an isolated cyclone could be represented by the following Gaussian function

$$f(x) = -e^{-a(x-L/2)^2}. \tag{4.4}$$

It is important to note that we only look at the field at one latitude at a time, which is the reason why we use a 1-D Gaussian in Equation 4.4.

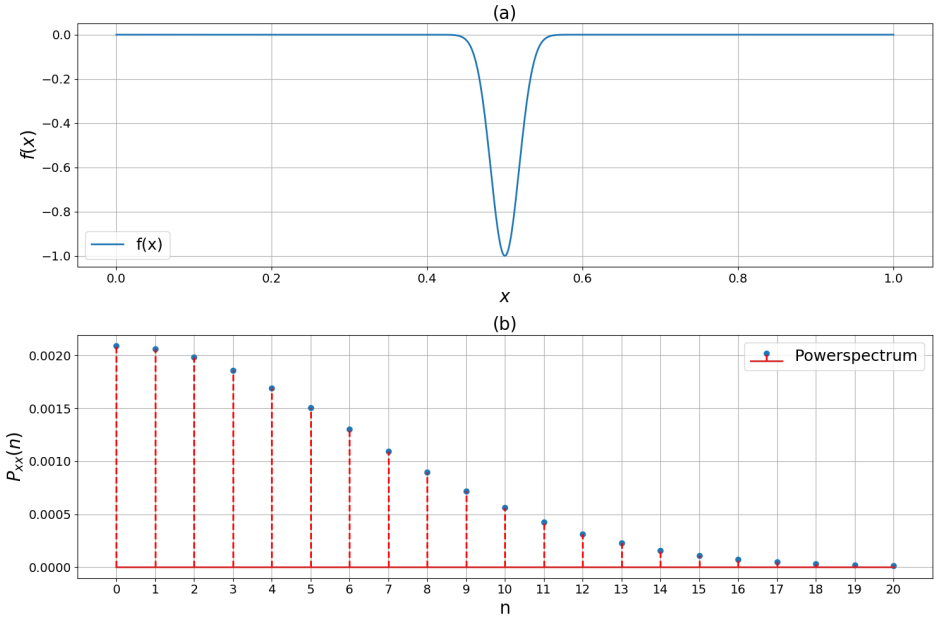

Figure 4.10: (a) - Plot of the waveform in Equation 4.4 and (b) - The power spectrum of the waveform in Equation 4.4.

From the power spectrum in Figure 4.10 we see that the power of the synoptic cyclone is spread across the wavenumbers representing both synoptic and planetary waves. This illustrates one source for possible errors in the ESM proposed by Graversen and Burtu (2016). Isolated synoptic events, like a single cyclone, propagate power to the low wavenumbers.

The velocity field of a single cyclone is not of the same shape as the depression in the pressure field itself. In two dimensions we would observe a circulation around the center of the cyclone. Across one single latitude the velocity field can be expressed by combining two Gaussian functions. This is done under the assumption that we have geostrophic balance, i.e. the pressure gradient is balanced by the Coriolis force in the horizontal momentum equations. Assuming geostrophic balance it is reasonable to represent the meridional velocity field of a single cyclone located at the center of the domain $x \in [0, L]$ as

$$f(x) = e^{-a(x-L/2-b)^2} - e^{-a(x-L/2+b)^2}, \tag{4.5}$$

where a is a constant determining how narrow each Gaussian is, and b is the displacement of the peaks from the middle of the domain.

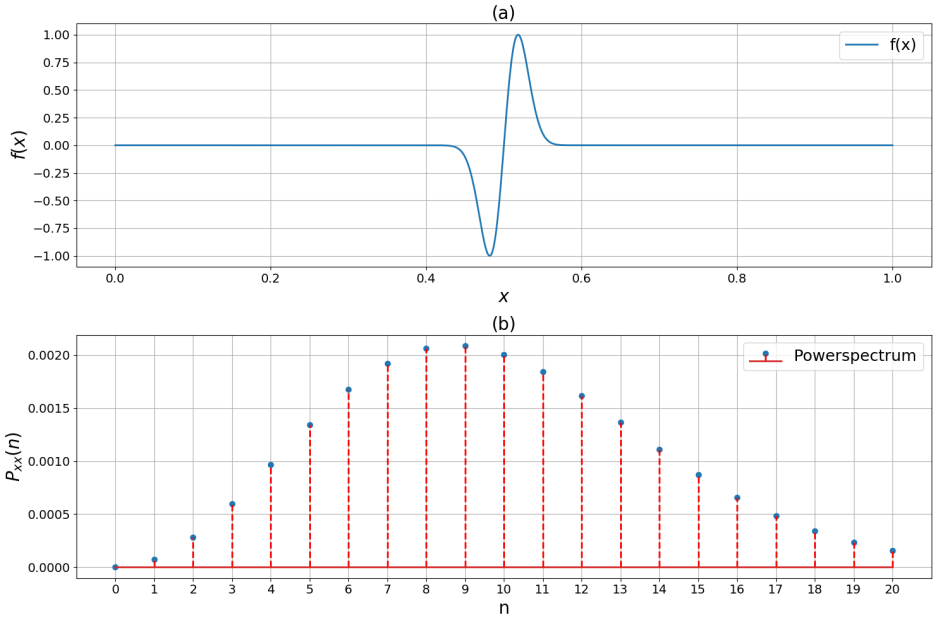

Figure 4.11: (a) - Plot of the waveform in Equation 4.5 and (b) - The power spectrum of the waveform in Equation 4.5.

The power of the components of the velocity field, Equation 4.5, of an isolated cyclone is spread across both the planetary and synoptic wavenumbers. From Figure 4.11 we see that the power spectrum peaks in the synoptic wavenumbers as opposed to the waveform in Figure 4.10, but we do still have a big portion of the power in the low wavenumbers. Thus a possible problem of the ESM is that power from isolated synoptic phenomena is spread to the low wavenumbers, even when there are no planetary phenomena present in the atmosphere.

4.3.2 Energy Transport due to Artificial Cyclones

The power spectrum of the waveform in Equation 4.5 suggests that power from a singular synoptic phenomenon, like a cyclone, could possibly propagate to low wavenumbers. To further explore whether or not this is the case we look at an idealization of a cyclone. The idealization for the geopotential height of the cyclone that we use is a Gaussian similar to the one in Equation 4.4. For the velocity field we assume that only the geostrophic winds are present. The meridional geostrophic winds are given as

$$v = \frac{g}{f}\frac{\partial z}{\partial x}, \tag{4.6}$$

where g is the gravitational acceleration, f is the latitude dependent Coriolis parameter, and z is the geopotential height. In reality we would have a geostrophic wind in the zonal direction as well, but under the assumption that we look at an idealized cyclone through its center in the zonal direction the zonal component will be omitted. Applying Equation 4.6 we compute the geostrophic wind associated with the idealized cyclone.

$$v_g = \frac{2ag}{f}(x - L)e^{-a(x-L)^2}. \tag{4.7}$$

In this specific case we look at the transport due to winds of the form in Equation 4.7 and a deviation in temperature from the mean field that has a shape similar to the one in Figure 4.11. We inspect the ESM for several different

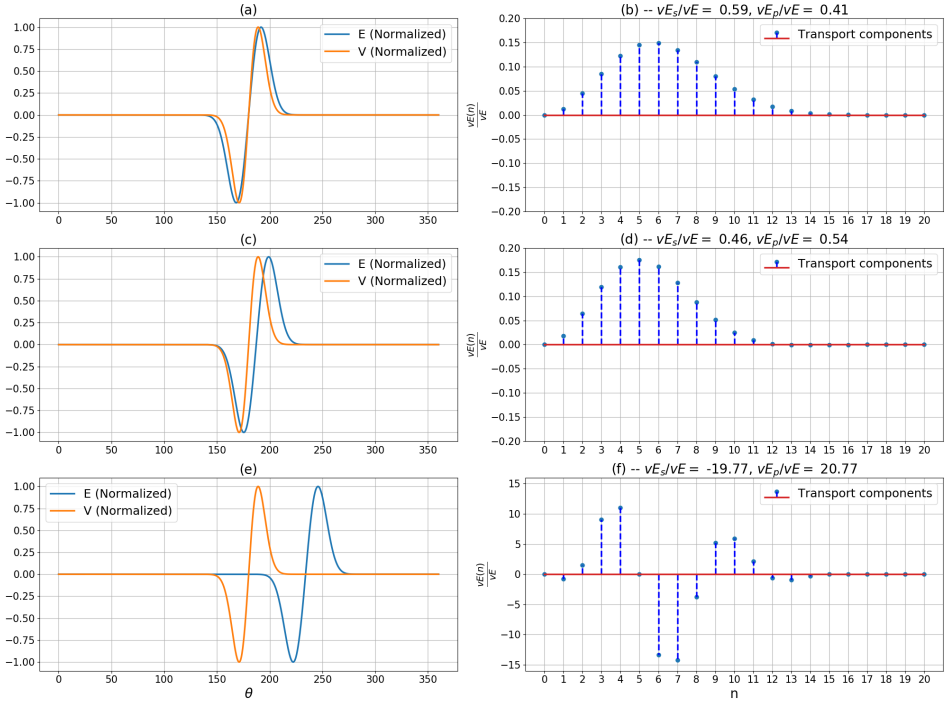

Figure 4.12: Plots of the Energy and Velocity field for the artificial cyclones for several relative phase shifts. The fields in (a) are not shifted. The transport components plotted in (b) corresponds to the transport in (a). In (c) the energy (Temperature) field has been shifted by $\phi = 7.2°$. The components in (d) corresponds to the fields in (c). The energy (Temperature) field in (e) has been shifted by $\phi = 54°$, and the components of the transport are plotted in (f). Note the scale difference between (b)/(d) and (f).

phase shifts of the two fields, in relation to each other. Both the velocity field in Equation 4.7 and the temperature field of the form given by Equation 4.5

are on synoptic length scales[1]. Thus, based on the fields alone, we should not expect to find any transport in the planetary wavenumbers. By inspecting the power spectrum of the temperature field, given in Figure 4.11, we see that there is a possibility of transport also in the planetary wavenumbers. In Figure 4.12 we have plotted the temperature and velocity fields for several different phase shifts, as well as the energy transport components corresponding to each of the cases.

The total transport is dependent of the phase between the temperature and velocity fields. We observe this from the computed transports in Figure 4.13 (c), which are relative to the maximum transport for a separation of planetary and synoptic waves between wavenumbers 5 and 6. The total transport is decreasing from Figure 4.12 (a) to Figure 4.12 (c), and has switched sign, while decreasing in magnitude, from Figure 4.12 (c) to Figure 4.12 (e).

The power spectra of the velocity and temperature fields remain constant even though the fields are shifted. But as we can observe from Figure 4.12 (b), (d), and (f) the fraction of the total transport for each of the transport components does not remain constant as we perform a phase shift. And even more importantly the synoptic and planetary fractions of the transport are changing. This change of transport components is arising from the mathematics of the ESM. As we perform a phase shift on the temperature field its power spectrum is staying constant, i.e. the power of each wavenumber will stay constant. But, the phase shift will affect the sign of the components. A single transport component is expressed as

$$vE_n = \frac{L}{2}\left(a_n^v a_n^E + b_n^v b_n^E\right), \tag{4.8}$$

where a_n^v and b_n^v are the Fourier coefficients of the velocity field, and b_n^E and a_n^E are the Fourier coefficients of the energy field (or temperature field in this specific case). As we phase shift the temperature field we know that the power spectrum will remain constant. This implies that for a specific component we will have that

$$P(E_n) = a_n^2 + b_n^2 = P(E_{ns}) = \text{constant}, \tag{4.9}$$

where $P(E_n)$ is the power of component n, and $P(E_{ns})$ is the power of the shifted component. The fact that the power spectrum remains constant does not imply that the coefficients a_n and b_n remain constant. From Equation 4.8 we see that a phase shift can lead to a decrease or increase of the specific component. This will happen even though the power of the component remains constant during the phase shift. The change of the magnitude of the transport components due to a phase shift does make physical sense, as the energy transport is dependent on the phase between v and E.

1. Length scales of order 1000km (Holton & Hakim, 2013)

Even more insight on how the fractions of transport are changing between synoptic and planetary waves as a function of the phase shift can be found by making a plot of the transport versus the phase. From Figure 4.13 we observe

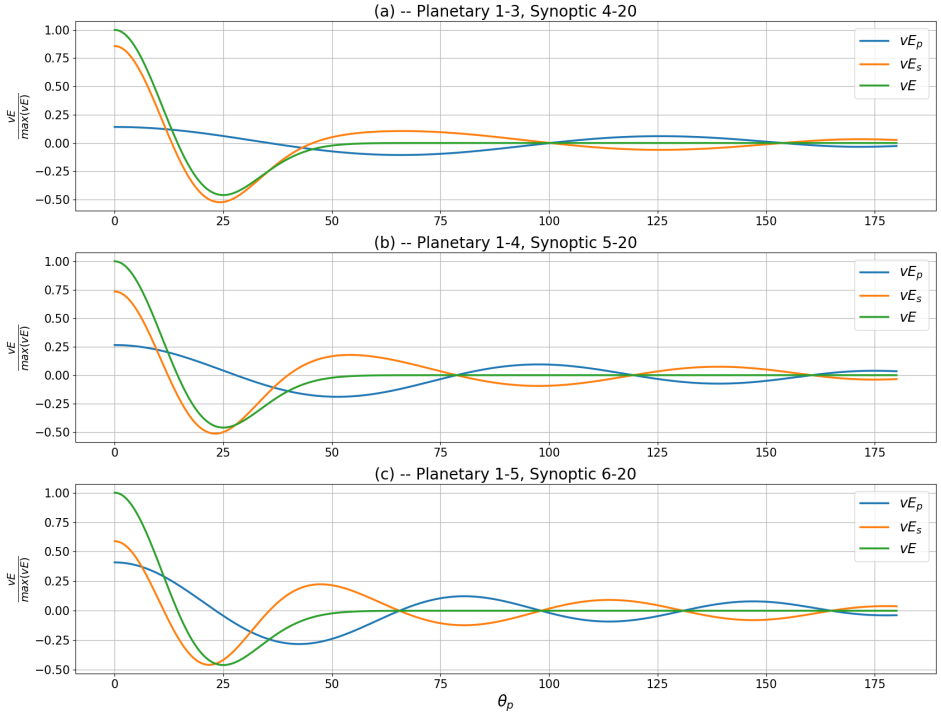

Figure 4.13: Plot of the planetary (vE_p), synoptic (vE_s) and total transports (vE) as functions of the relative phase shift between v and E, in the range $\theta_p \in [0°, 180°]$. The subplots (a) – (c) are distinguished by different separations of planetary and synoptic waves. In (a) the planetary range is defined as the wavenumbers 1-3, in (b) as the wavenumbers 1-4, and in (c) as the wavenumbers (1-5). The synoptic range is the remaining wavenumbers up to $n = 20$. The angle θ_p plotted on the x-axis represents the longitudinal phase shift of the energy (temperature) field.

that the fraction of the transport due to planetary waves is dependent on the phase shift between the fields. This can be explained by the fact that the overlap between wave components will vary with the phase shift. From Figure 4.13 we also observe that the fractions of planetary versus synoptic transport are highly dependent on the threshold where we separate between the planetary and synoptic scale. As noted in both Peixoto and Oort (1992) and Graversen and Burtu (2016) the wavenumber threshold at which we separate between synoptic and planetary waves is somewhat arbitrary. It is suggested that the threshold is between wavenumber 5 and 6, but this is not an absolute definition. In the study of this single event, without planetary waves present, it is reasonable to expect that the planetary transport should be low. From the

examples in Figure 4.12 and Figure 4.13 we see that this is not the case. But, from Figure 4.13 we can deduce that the magnitude of the planetary transport is dependent on the planetary-synoptic threshold chosen. Choosing a threshold between wavenumber 5 and 6, as done in Graversen and Burtu (2016), the planetary transport in this idealized case reaches 0.41 times the total transport maximum. The planetary transport will account for all of the transport for some phase shifts, but in these cases the total transport is only ~ 0.3 times the transport maximum. This is ~ 2.92 times the maximum planetary transport reached with a threshold between wavenumber 3 and 4, which is 0.14 times the transport maximum. Even a threshold set between wavenumber 4 and 5 results in a significantly lower planetary transport fraction when the transport is at a maximum. The planetary transport in this case has a maximum of 0.26 times the transport maximum, which is 0.63 times the maximum planetary transport reached with a threshold between wavenumbers 5 and 6.

For all three thresholds between planetary and synoptic waves we see that the ESM has problems resolving the energy transport induced by the isolated cyclone. The energy transport is localized in the region where we have the artificial cyclone. But due to the fact that the associated wind field is resolved such that there is power in both planetary and synoptic wavenumbers we will get transport in the planetary waves, which are not present in the synthetic atmosphere.

5

Mean Energy Transport Fields

5.1 Dependence on Thresholds *T* and *C*

The mean energy transport fields, in terms of wavenumbers, for specific atmospheric patterns give us insight in how the ESM resolves the transport patterns associated with these specific cases. In this chapter we will look at various mean transport field decompositions, for atmospheric patterns found through filtering algorithms. We apply the conditional cyclone filter described in Chapter 3 at 70° north, and inspect how the cyclone threshold C and the threshold for deviations from the mean T (Figure 3.1) affect the mean transport field components and magnitude.

One would expect that the planetary transport should decrease, whilst the synoptic transport should increase when we increase C, since the synoptic cyclone depression is increasing in strength with C. From Figure 5.1 we see that this is not the case. The planetary transport is actually increasing as C is increased. The behavior of the synoptic transport is not as straightforward. The synoptic transport is not changing much until we reach $C \approx 265$m, from which the synoptic transport is increasing rapidly for small T and decreasing for large T. The synoptic transport flattens for small T when we reach $C \approx 285$, whilst the transport for large T starts increasing from here. The increase in the overall transport as a function of C may be related to seasonal variations in the

geopotential height field. When C is high, we will get fewer cases marked as cyclones, as seen in Table 5.1. These cases will most likely be from the winter months, when the dry static transport energy is high due to the enhanced temperature gradient between the poles and the equator (Holton & Hakim, 2013). From Figure 5.1 we see that for the interval $T \approx 77$m to $T \approx 92$m the energy transport is behaving differently than for the rest of the values of T. In this interval the planetary transport is varying more than for the rest of the cases, and the synoptic transport is much greater than for the other cases. There are multiple possible explanations for this, one of which is that since these are the strongest constraints on the field outside the cyclone region we will get fewer cases of interest when T is in this interval. This leads to great variation in the transport field when we increase C since the characteristics of the individual cases are more present as we average over fewer cases. Not only

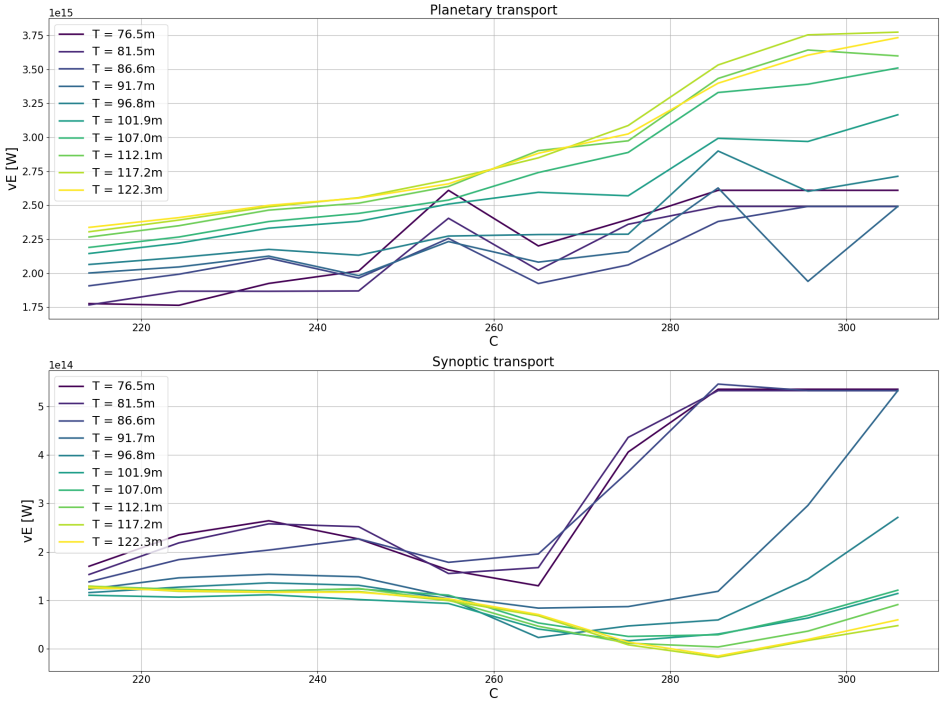

Figure 5.1: Mean planetary and synoptic dry static energy transport, separated between wavenumbers $n = 5$ and $n = 6$, as a function of C for several values of threshold T. Note the scale difference between Planetary and Synoptic scale transport.

is the planetary wave transport increasing with C, it is also greater for large values of T than for small values of T. The increase of planetary transport with T seems reasonable. A high T-value in the filter allows larger deviations from the mean outside the cyclone region, which is a weaker constraint on the planetary waves than a low T-value. Thus it is evident that large T-values is consistent

with more planetary wave activity than in the case of small T-values.

In the low range of T we observe that the synoptic transport is increasing with C. This is what we would expect based on the physics of the atmosphere: with a stronger depression in the geopotential height the meridional geostrophic winds will increase, thus providing conditions where more energy can be transported across a latitude by the cyclone. It is important to note that the y-scale of planetary transport in Figure 5.1 is one order of magnitude higher than the y-scale of the synoptic transport. This means that for all the cases considered the planetary transport is much greater than the synoptic transport. This is illustrated by the fractions of total transport plotted in Figure 5.2.

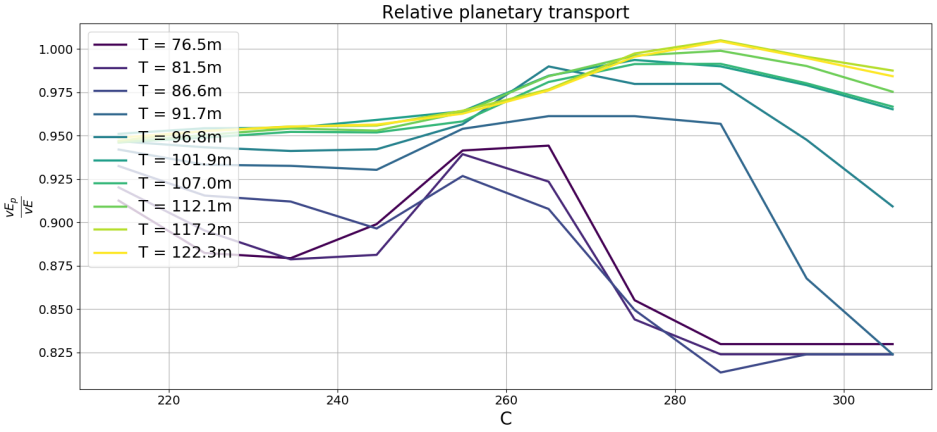

Figure 5.2: Mean planetary dry static energy transport as a fraction of the total eddy transport. Separation between planetary and synoptic waves between $n = 5$ and $n = 6$. The transport is plotted as a function of C for multiple values of threshold T.

The planetary wave transport contributes between to over 80% of the total transport, whilst the synoptic transport is responsible for the rest. The filter used is selecting cases where we have isolated synoptic phenomena. For the weakest constraints in C and T the filter will likely pass through cases where there is planetary wave-activity present. But for the strongest constraints the synoptic scale phenomena should by construction be the most prominent feature in the 850hPa geopotential height field. In the cases with the strongest conditions in C and T, the planetary transport fraction is at a minimum, although it still is contributing to over 80% of the dry static energy transport. A possible explanation for the large fraction of planetary transport, when we have only strong synoptic phenomena present in the atmosphere, is that the synoptic phenomena are only transporting energy locally. Whilst the planetary phenomena, although weak, can transport energy across a whole latitude circle. This means that even though the most prominent feature in the cases we consider is the depression in the geopotential height we cannot be sure

that the main portion of the meridional energy transport will be induced by the depression in the geopotential height field. Another possibility is that the ESM is resolving the fields incorrectly and is thus accounting some of the synoptic transport as planetary transport. Based on the results of Section 4.3, where synoptic transport is projected on to the planetary waves, the incorrect resolution of the fields is a possible explanation for the large fraction of planetary transport in these specific cases.

Table 5.1: The number of cases, n, for each T and C (in meters).

C \T	71.4	76.5	81.5	86.6	91.7	96.8	101.9	107.0	112.1	117.2	122.3
203.9	45	68	112	166	253	352	508	694	899	1159	1468
214.1	31	47	73	111	181	246	350	494	641	827	1046
224.3	20	30	44	70	119	163	239	346	456	597	759
234.5	13	20	28	44	78	107	157	236	323	430	548
244.6	9	12	18	27	51	72	114	171	231	300	389
254.8	6	9	12	15	32	46	79	116	155	203	267
265.0	5	6	8	11	22	29	56	78	103	136	174
275.2	2	3	4	7	16	19	37	52	68	86	116
285.4	1	2	3	4	10	12	24	36	46	56	74
295.6	1	2	3	3	5	7	16	25	32	39	54
305.8	1	2	3	3	3	4	12	18	23	28	36

5.2 Mean Vertically Integrated Energy Transport

From Figure 5.2 we see that the ESM yields a remarkably high planetary fraction, 80% or more, of the dry static energy transport in all the cases we have considered. In this section we inspect the vertically integrated transport across 70° north for some of the cases considered earlier. When only performing the vertical integral, and not computing the zonal mean, we get a longitude dependent field. Here we consider total transport, and not the transport decomposed into waves. Thus we can compare the geopotential height field and the transport across the whole latitude circle, and check how the patterns coincide. The cases we have filtered are assumed to have the strong synoptic-scale depression in geopotential height localized in the cyclone region as the defining characteristic. In this section we will consider a split of the meridional energy transport not into wave components, but into the transport inside the cyclone region and outside the cyclone region. The transports considered in this section are defined as

vE_{Cr} : Transport inside the cyclone region,
vE_R : Transport outside the cyclone region,
vE_T : Total transport.

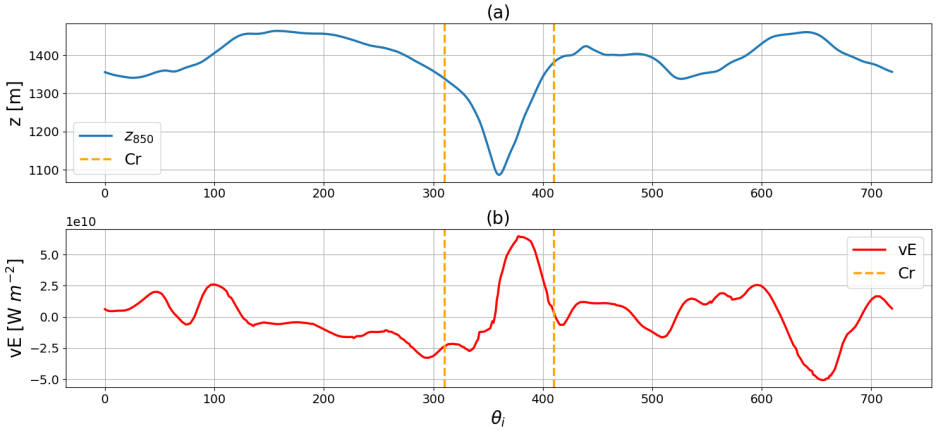

Figure 5.3: (a) – 850 hPa geopotential height for one of the cases with $C = 305.8$m and $T = 101.9$m.
(b) – Vertically integrated dry static energy transport corresponding to the geopotential height field in (a). θ_i is the grid points in the longitude direction.

In addition to the actual transports we consider zonal means of the transports. The zonal means of vE_{Cr} and vE_R are constructed respectively by setting the transport outside and inside the cyclone region equal to zero, and then computing the mean of the field. This is done to ensure that the transport is divided by the same number of samples, such that the mean transports are comparable. In addition this ensures that $\overline{vE_{Cr}} + \overline{vE_R} = \overline{vE_T}$, i.e. that the sum of the zonal mean of the transport inside and outside the cyclone region equals the zonal mean of the transport.

From Figure 5.3 we observe that the maximum of the meridional dry static energy transport is located inside the cyclone region. The transport peak is located just to the right of the cyclone center, this is described by the fact that the meridional winds will be northward and at their strongest just to the right of the cyclone center. The zonal mean transports for the specific case in Figure 5.3 are $\overline{vE_{Cr}} \approx 3.04 \times 10^9 \text{W m}^{-2}$ and $\overline{vE_R} \approx -2.99 \times 10^9 \text{W m}^{-2}$. We see that the zonal mean of the transport inside the cyclone region, $\overline{vE_{Cr}}$, is a bit greater in magnitude than the zonal mean outside the cyclone region, $\overline{vE_R}$, but the signs are opposite. Keeping in mind the fact that the cyclone region is much smaller than the rest of the region, it is worth noting that the magnitude of $\overline{vE_{Cr}}$ is greater than that of $\overline{vE_R}$. This means that if the transport localized in the cyclone region was spread across the whole latitude circle, the transport would still have a greater magnitude than if we spread the transport outside the cyclone region across the whole latitude circle. The total zonal mean energy transport is given as $\overline{vE_T} = \overline{vE_{Cr}} + \overline{vE_R} \approx 5 \times 10^7 \text{W m}^{-2}$, which is two orders of magnitude less than both $\overline{vE_{Cr}}$ and $\overline{vE_R}$. The magnitude difference between

$\overline{vE_T}$ and $\overline{vE_{Cr}}$ is not surprising, since $\overline{vE_{Cr}}$ and $\overline{vE_R}$ are of the same magnitude with opposite signs and $\overline{vE_T} = vE_{Cr} + \overline{vE_{Cr}}$.

From one case, like in Figure 5.3, we gain insight in how the system we consider works, but we cannot draw quantitative conclusions from one case. In Table 5.2 we have considered the mean fraction $\frac{\overline{vE_{Cr}}}{\overline{vE_T}}$ for all the cases found by the conditional filter for the specified C and T values. From the data presented in

Table 5.2: The mean fraction of the zonal mean transport inside the cyclone region, $\overline{vE_{Cr}}$, compared with the total zonal mean, $\overline{vE_{Cr}}$.

C \T	71.4m	76.5m	81.5m	86.6m	91.7m	96.8m	101.9m	107.0m	112.1m	117.2m	122.3m
203.9m	20.35	14.87	19.12	18.75	20.42	18.24	16.54	15.98	14.55	13.75	12.83
214.1m	22.73	17.31	23.62	21.88	23.69	21.22	19.00	17.30	16.37	15.47	14.03
224.3m	28.27	21.11	17.64	15.79	21.62	17.99	16.58	15.42	15.33	15.02	13.98
234.5m	30.68	21.93	13.90	14.90	24.87	20.33	17.81	16.49	16.59	15.41	14.00
244.6m	27.59	23.98	13.27	14.87	30.53	23.83	20.74	17.21	17.60	15.99	14.47
254.8m	17.18	15.84	12.84	12.82	39.94	28.22	22.45	18.96	19.78	15.66	13.45
265.0m	19.76	19.23	14.13	13.76	5.81	2.35	8.51	8.58	12.94	10.20	7.56
275.2m	22.52	20.54	13.17	12.99	4.17	0.96	6.43	9.35	8.62	9.45	6.16
285.4m	10.51	13.54	6.05	10.56	11.84	15.13	11.92	13.78	11.68	12.42	6.53
295.6m	10.51	13.54	6.05	6.05	2.41	10.76	12.80	14.74	12.94	13.78	5.59
305.8m	10.51	13.54	6.05	6.05	6.05	15.31	12.47	14.96	12.15	12.81	13.38

Table 5.2 we observe that for a large fraction of the values C and T, $\overline{vE_{Cr}}$ is approximately one order of magnitude greater than the total zonal mean $\overline{vE_T}$. In other words, if we only had the transport across the cyclone cross section present in the energy transport field, the zonally mean energy transport would be ~ 10 times as great as the total zonal mean. The zonal means inside and outside the cyclone region are related to the total zonal mean through the expression in Equation 5.1.

$$\overline{vE_T} = \overline{vE_{Cr}} + \overline{vE_R}. \tag{5.1}$$

Dividing Equation 5.1 by $\overline{vE_T}$ yields

$$\frac{\overline{vE_{Cr}} + \overline{vE_R}}{\overline{vE_T}} = \frac{\overline{vE_{Cr}}}{vE_T} + \frac{\overline{vE_R}}{vE_t} = 1. \tag{5.2}$$

From Equation 5.2 we see that the fraction $\frac{\overline{vE_R}}{\overline{vE_T}}$ has to be of the same order of magnitude as the fractions in Table 5.2, but with the sign flipped. Based on Table 5.2 the transport inside the cyclone region is contributing to a significant portion of the total transport. Especially since the transports compared are averaged over the whole latitude circle, whilst the cyclone region is only a small fraction of the total distance.

The cyclone region is small compared to the total length over a latitude circle. But the transport inside the cyclone region is large. By comparing the means of

the transport inside and outside, not zonal means, we take into consideration the length scale differences between the regions. This gives us a view of how the fraction per grid point inside and outside the cyclone region behaves as we vary C and T.

Table 5.3: Absolute mean fraction of the mean dry static energy transport inside the cyclone region relative to the transport outside the cyclone region.

C \T	71.4m	76.5m	81.5m	86.6m	91.7m	96.8m	101.9m	107.0m	112.1m	117.2m	122.3m
203.9m	6.78	6.74	6.68	6.77	42.74	32.9	25.51	20.47	17.33	15.03	13.38
214.1m	6.75	6.62	6.6	6.74	56.68	43.48	33.48	25.7	21.37	18.07	15.77
224.3m	6.84	6.67	6.67	6.86	6.86	6.8	6.78	6.82	6.83	6.79	6.85
234.5m	6.77	6.66	6.53	6.87	6.8	6.74	6.64	6.73	6.73	6.74	6.74
244.6m	6.86	6.83	6.62	6.96	6.77	6.73	6.6	6.6	6.67	6.65	6.68
254.8m	7.02	6.93	6.82	7.48	7.04	6.93	6.63	6.68	6.67	6.63	6.66
265.0m	6.8	6.77	6.69	7.62	7.22	7.02	6.61	6.77	6.68	6.66	6.71
275.2m	6.62	6.61	6.35	7.97	7.39	7.22	6.66	6.93	6.73	6.66	6.57
285.4m	6.85	6.73	6.34	6.37	6.47	6.46	6.23	6.72	6.58	6.58	6.52
295.6m	6.85	6.73	6.34	6.34	6.36	6.38	6.3	6.42	6.46	6.52	6.47
305.8m	6.85	6.73	6.34	6.34	6.34	6.34	6.26	6.38	6.43	6.51	6.47

In Table 5.3 we have compared (taken the fraction of) the mean dry static energy transport inside the cyclone region with the transport outside of the cyclone region. We observe that the mean dry static energy transport inside the cyclone region is larger than the transport outside the cyclone region for all the cases considered. The mean absolute fraction, mean of all values in Table 5.3, is ~ 9.10. Thus more dry static energy is transported inside the cyclone region in average than outside the region, for all values of C and T.

Until now we have only considered the dry static energy transport. To see the whole picture we have to consider the latent heat transport as well. We show only the values for the comparison of mean latent heat transport inside and outside the cyclone region, not the comparison of the zonal means. From

Table 5.4: Mean latent heat transport fraction of transport inside the cyclone region relative to the transport outside the region.

C \T	71.4m	76.5m	81.5m	86.6m	91.7m	96.8m	101.9m	107.0m	112.1m	117.2m	122.3m
203.9m	5.64	5.78	4.48	8.49	6.91	7.57	7.36	7.25	6.2	5.35	13.74
214.1m	7.4	7.75	5.44	11.52	8.73	8.23	8.05	8.14	6.98	5.96	17.83
224.3m	10.26	7.46	5.31	4.54	5.02	6.02	7.22	8.1	6.86	5.78	22.55
234.5m	10.77	7.4	5.47	5.02	6.03	7.74	9.15	10.13	8.02	6.63	29.99
244.6m	9.73	7.78	5.37	5.63	7.45	10.14	11.44	12.88	10.24	8.6	41.25
254.8m	13.51	9.64	7.45	6.51	9.47	13.52	12.39	9.87	8.21	6.79	55.44
265.0m	16.2	13.85	10.69	8.52	12.54	10.13	11.49	9.93	8.33	6.9	82.02
275.2m	32.19	22.16	16.65	10.68	15.94	14.06	15.17	12.75	10.56	8.87	121.5
285.4m	8.83	5.46	3.68	3.7	18.66	16.07	9.11	8.7	7.39	6.51	176.9
295.6m	8.83	5.46	3.68	3.68	2.27	2.52	2.36	2.03	2.32	2.22	237.15
305.8m	8.83	5.46	3.68	3.68	3.68	2.83	2.34	2.16	2.38	2.19	2.56

Table 5.4 we observe that the magnitude of the latent heat transport inside the

cyclone region is greater than the transport outside the region. The mean of the absolute fractions of the latent heat transport for the cases we have considered is ~ 14.10. This is greater than the mean of the absolute fraction of the dry static energy transport. This indicates that in general a strong depression in the geopotential height will contribute to a larger fraction of the total transport of latent heat than dry static energy. Inspecting the ESM of the relative latent heat transport in a similar way as in Figure 5.2 we find that the planetary transport of latent heat is greater than 70% of the total transport in the considered cases. If this were to be the case we would expect the fraction between transport inside and outside the cyclone region to be smaller than it is.

From the investigations in this section it is evident that the transport, of both latent heat and dry static energy, inside the cyclone region is large compared with the transport outside of the cyclone region, in the considered cases. From the ESM we find that, for the same cases, the planetary waves are contributing to the main portion of the energy transport. This is not in agreement with the result that the largest fraction of the energy transport occurs in the cyclone region, which suggests that it is the synoptic phenomenon that transports the largest portion of the energy.

5.3 Statistical Significance of Mean Transports

The results in the previous section indicate that the transport, per grid point, around the strongest depression in the geopotential height field is greater in magnitude than the transport in the remainder of the domain. To test whether or not the transport fraction is different from the normal state of the atmosphere we test the statistical significance of the transport fractions by applying a Monte-Carlo approach (Section 3.4). For each pair of C and T we pick a random sample of time points in the data set that equals the number of cases the conditional filter has found for the specific pair of C and T. The samples chosen are not completely random, they are restricted such that they consist of the same amount of data for each month as the filtered cases. This is done to ensure that what we test is not the transport in different months, but the transport for a random combination of cases from the same months as the filtered data. To test the statistical significance of the transport fractions in Table 5.3 and Table 5.4 a large number of random samples is generated, and the transport fractions of these random samples are compared with the fractions for the filtered cases. The hypothesis we test is that the mean magnitude of the transport inside the cyclone region compared with the transport outside the cyclone region is greater for the filtered cases than for a random field.

The statistical significance of the absolute mean transport fractions is computed

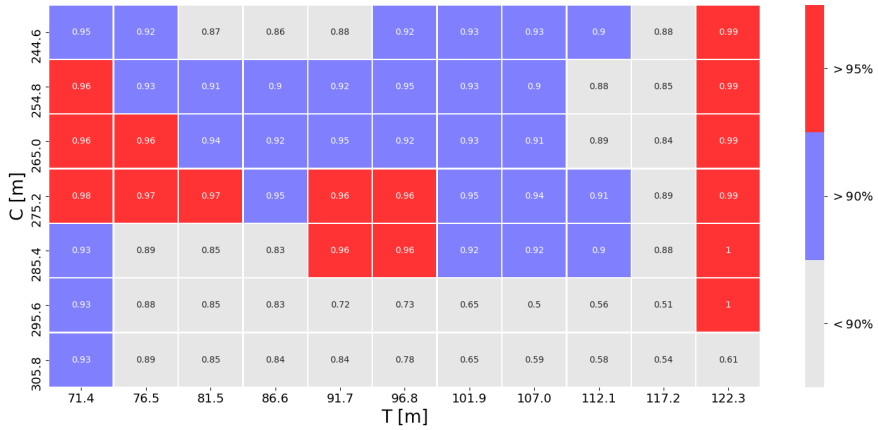

Figure 5.4: Significance of the relative mean transport of latent heat in the cyclone region compared with the transport outside the cyclone region. The significance has been tested for several values of thresholds C and T. The significance is determined by the color (and value) in each cell, where the red cells are significant on a 95% level, blue cells on a 90% level, and gray cells are not statistically significant. The significance test has been performed by 3000 iterations of the Monte Carlo method.

by comparing the filtered transport fractions with those of the random fractions, summing all the samples when the filtered transport fraction is greater than the random fraction, and then dividing by the number of random samples. This gives an estimate of the percentage of the comparisons where the filtered field will be greater than the random field. We say that the transport fraction of the filtered filter is significant on e.g. a 95% level if the percentage is over 95%. The percentages are shown in Figure 5.4 and Figure 5.5.

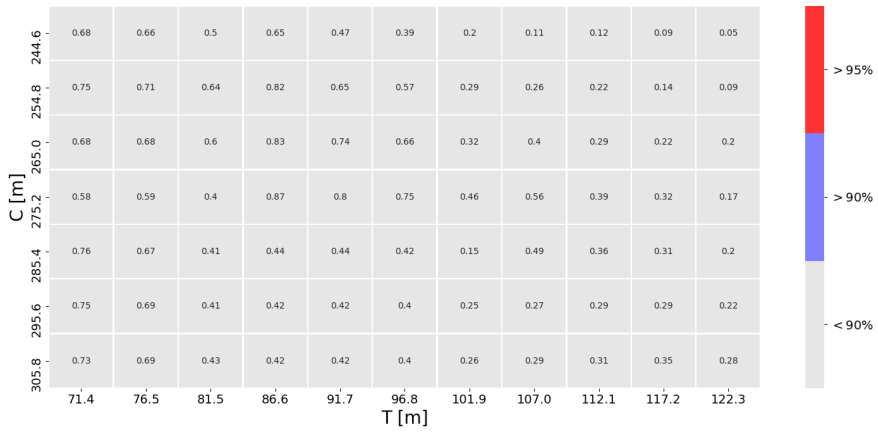

Figure 5.5: As in Figure 5.4 but for the relative mean transport of dry static energy.

From Figure 5.4 it is evident that the fraction of the mean latent heat transport inside the cyclone region compared with the rest of the field is greater for the filtered fields than for the the random fields in the majority of the cases. Even more interestingly the transport fraction of dry static energy does not differ much from the fractions computed for the random fields, which can be observed from Figure 5.5. This implies that the transport of latent heat inside the cyclone region is different from that of random cases, whilst the dry static energy transport could just as well be due to a random field.

Until now we have only considered the absolute mean fractions of cyclone region transport compared with transport outside the cyclone region. We have not tested whether or not the mean energy transport inside the cyclone region is significant, relative to the climatology, for the filtered cases. To test the significance of the mean transports inside the cyclone region we apply a similar Monte Carlo approach as earlier.

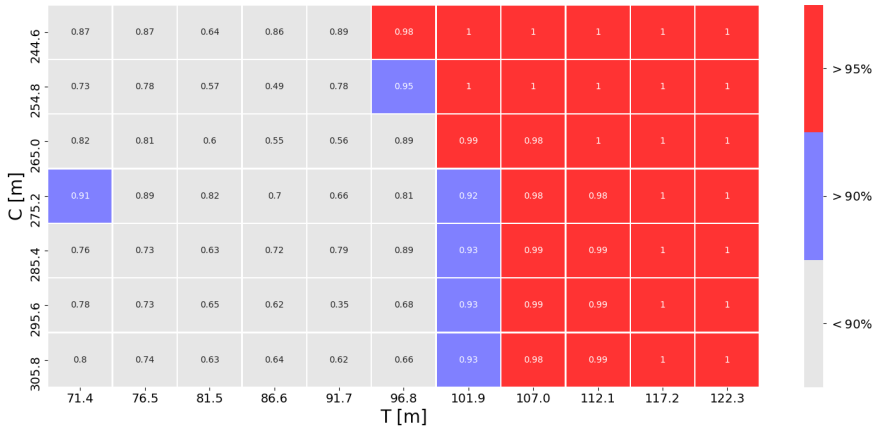

Figure 5.6: As in Figure 5.4 but for the mean transport of dry static energy inside the cyclone region.

From Figure 5.6 it is evident that the cyclone region dry static energy transport is highly significant when C is on the lower end and T on the higher end of the scales. When T is high the field outside the cyclone region is less constrained. In combination with the fact that C is in the low end for most of the significant cases this could actually indicate that there are planetary waves present in the atmosphere in these situations. The fact that the significance of the fraction of cyclone region dry static transport compared with the transport outside the cyclone region is small in the same cases provides a strong indication that there are in fact planetary waves present in these situations.

The transport of latent heat inside the cyclone region is significantly larger than the climatology on a 90% level for all but two of the considered situations.

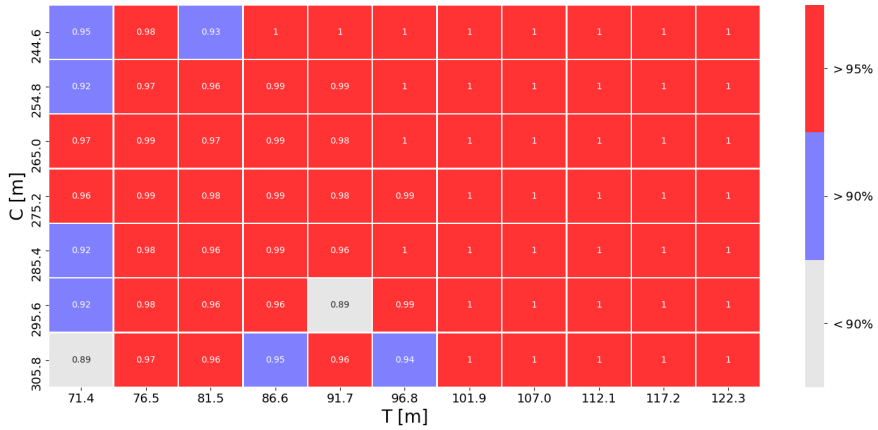

Figure 5.7: As in Figure 5.4 but for the mean transport of latent heat inside the cyclone region.

In addition the absolute mean fraction of the latent heat transport inside the cyclone region compared with the transport outside the cyclone region is significant on a similar level for a large fraction of the considered cases. This indicates that cyclones actually are contributing to a significant portion of the transport of latent heat. A possible explanation for the significance of latent heat transport is the fact that the humidity of air is exponentially dependent on the temperature, as stated in the Clausius-Clapeyron relation (Vallis, 2017). Thus a small temperature difference has large effects on the humidity of the air. This indicates that the latent heat transport can be large even when the temperature difference is small. This will not be the case for the dry static energy since sensible heat is an important term in the transport, and the sensible heat is linearly proportional to the temperature.

The large contribution to the latent heat transport due to cyclones does not agree with what we get from the ESM in these special cases, where above 70% of the transport is accounted for by planetary waves.

6

Summary & Concluding Remarks

6.1 Summary

In this study we have attempted to answer the question of how well the ESM, proposed in Graversen and Burtu (2016), works for representing the meridional energy transport contributions of waves. Applying the ESM on synthetic data (Chapter 4) reveals that the ESM has problems with resolving isolated and localized synoptic events. Transport localized around a synthetic cyclone is resolved into transport both in the planetary and synoptic waves. Applying the conditional filter (Chapter 3) on the 850hPa geopotential height field from the ERA-Interim dataset yields several cases where a single depression is the main characteristic of the field (Table 5.1). In these cases the ESM yields a split where over 80% of the dry static eddy transport and over 70% of the latent heat eddy transport are in the planetary range (Chapter 5).

Inspecting the vertically integrated meridional energy transport we uncovered the fact that energy transport in the cyclone region is greater per grid point than outside the region for all cases found by applying the conditional filter. Through the significance testing of the energy transport, we found that the latent heat transport in the cyclone region is statistically significant, on a 90% level, for all but two thresholds C (cyclone threshold) and T (variability threshold) (Figure 5.7), whilst the dry static energy transport is only significant

for weak constraints in the threshold T (Figure 5.6).

For the latent heat the fraction of transport inside compared with the transport outside the cyclone region is shown to be great in magnitude and of statistical significance (Table 5.4 and Figure 5.4). The similar fraction of the dry static energy transport is also large but is not statistically significant compared to that of random samples (Table 5.3 and Figure 5.5). This indicates that cyclones transport a significant amount of latent heat poleward at 70° north, but are not contributing significantly to the transport of dry static energy.

To pick out situations categorized as isolated cyclones a conditional filter was developed. The filter selects cases based on simple constraints on the geopotential height field. A possible weakness of the filter is that it might select cases with planetary waves when the constraints are too weak. It is likely that this has happened for the weak constraints C and T in this study. This study has also only been conducted at 70° north, and should be conducted at more latitudes to strengthen our confidence in the results. Another possible source of inaccuracy in this study is the separation of transport inside and outside the cyclone region in Chapter 5. If the applied filter allows for planetary waves to exist these might transport energy in the cyclone region as well as outside of it. Thus the quality of the filter is one of the main sources of misinterpretation in this study. In this study we have not emphasized the ability of the ESM to resolve the transport when the atmospheric state is dominated by waves in the planetary range. This has only been partly tested with some of the simple waveforms in Chapter 4 where no indication of problems was found. This should still be further tested to make sure that problems do not arise when resolving planetary phenomena.

6.2 Future Work

A natural next step would be to expand the study to cases found by applying a different filter. A spherical harmonics filter could be applied. Even though a spherical harmonics expansion relies on sinusoids it is not equivalent to the zonal Fourier decomposition. In this study only cases with isolated cyclones are investigated. The approach through spherical harmonics could be applied to test the ESM in cases were both cyclone scale waves and Rossby waves are present in the atmosphere. Filtering for cyclones through a wavelet transform is another approach that could be sought, since these are localized in space. Eventually one could try to develop a similar energy split method through wavelet transforms, and compare with the results of the ESM.

Another approach for future investigations is to perform the ESM on an at-

mosphere where the large waves are completely removed. The results of this could be used to estimate an upper limit to the error of the ESM, as the total transport contribution of the low wavenumbers in the remaining field could be considered as an upper error of the ESM. From the investigations of the synthetic data we found that a change of the planetary-synoptic wavenumber threshold from 5-6 to 4-5, or even 3-4, reduces the problem of resolving synoptic phenomena. Thus a possible future path would be to reproduce the investigations in Graversen and Burtu (2016) with a wavenumber threshold between 4-5 or 3-4, and compare these to the original study.

In this study we have not considered possible errors of the transport contribution of pure planetary waves. Even though the investigations of artificial data suggest that there will not be as large errors as for synoptic phenomenon an investigation into the planetary waves could be pursued.

6.3 Concluding Remarks

During this study we found that the ESM has problems resolving isolated synoptic phenomena. This is due to the fact that the atmospheric state in these cases resembles more a sharp Gaussian than pure sinusoidal waveforms. The significance of this error is especially of importance for the latent heat transport which affects the Arctic strongly (Graversen & Burtu, 2016; Messori et al., 2018). The role of cyclones in the latent heat transport has earlier been uncovered in Messori et al. (2018) where it is shown that cyclones are important contributors to moisture intrusions into the Arctic. For the filtered cases we did not find a significantly enhanced transport of dry static energy in the cyclone region, which diminishes the importance of the error in the ESM when considering the dry static energy transport.

Bibliography

Anderson, D., Hodges, K. I., & Hoskins, B. J. (2003). Sensitivity of feature-based analysis methods of storm tracks to the form of background field removal. *Monthly Weather Review*, *131*(3), 565-573. Retrieved from https://doi.org/10.1175/1520-0493(2003)131<0565:SOFBAM>2.0.CO;2 doi: 10.1175/1520-0493(2003)131<0565:SOFBAM>2.0.CO;2

Cohen, J., Screen, J. A., Furtado, J. C., Barlow, M., Whittleston, D., Coumou, D., ... Jones, J. (2014, Aug 17). Recent arctic amplification and extreme mid-latitude weather. *Nature Geoscience*, *7*, 627 EP -. Retrieved from https://doi.org/10.1038/ngeo2234 (Review Article)

Dee, D. P., Uppala, S. M., Simmons, A. J., Berrisford, P., Poli, P., Kobayashi, S., ... Vitart, F. (2011). The era-interim reanalysis: configuration and performance of the data assimilation system. *Quarterly Journal of the Royal Meteorological Society*, *137*(656), 553-597. Retrieved from https://rmets.onlinelibrary.wiley.com/doi/abs/10.1002/qj.828 doi: 10.1002/qj.828

Donohoe, A., & Battisti, D. S. (2009). The amplitude asymmetry between synoptic cyclones and anticyclones: Implications for filtering methods in feature tracking. *Monthly Weather Review*, *137*(11), 3874-3887. Retrieved from https://doi.org/10.1175/2009MWR2837.1 doi: 10.1175/2009MWR2837.1

Graversen, R. G. (2006). Do changes in the midlatitude circulation have any impact on the arctic surface air temperature trend? *Journal of Climate*, *19*(20), 5422-5438. Retrieved from https://doi.org/10.1175/JCLI3906.1 doi: 10.1175/JCLI3906.1

Graversen, R. G., & Burtu, M. (2016). Arctic amplification enhanced by latent energy transport of atmospheric planetary waves. *Quarterly Journal of the Royal Meteorological Society*, *142*(698), 2046-2054. Retrieved from https://rmets.onlinelibrary.wiley.com/doi/abs/10.1002/qj.2802 doi: 10.1002/qj.2802

Graversen, R. G., Mauritsen, T., Tjernström, M., Källén, E., & Svensson, G. (2008, Jan 03). Vertical structure of recent arctic warming. *Nature*, *451*, 53 EP -. Retrieved from https://doi.org/10.1038/nature06502

Holton, J. R., & Hakim, G. J. (2013). *An introduction to dynamic meteorology* (fifth ed.). 225 Wyman Street, Waltham, MA 02451, USA: Academic Press.

Hwang, Y.-T., Frierson, D. M. W., & Kay, J. E. (2011). Coupling between arctic feedbacks and changes in poleward energy transport. *Geophysical Research Letters*, *38*(17). Retrieved from https://agupubs.onlinelibrary.wiley.com/doi/abs/10.1029/2011GL048546 doi: 10.1029/2011GL048546

IPCC. (2013). Summary for policymakers [Book Section]. In T. Stocker et al. (Eds.), *Climate change 2013: The physical science basis. contribution of working group i to the fifth assessment report of the intergovernmental panel on climate change* (p. 1–30). Cambridge, United Kingdom and New York, NY, USA: Cambridge University Press. Retrieved from www.climatechange2013.org doi: 10.1017/CBO9781107415324.004

Kay, J. E., Holland, M. M., Bitz, C. M., Blanchard-Wrigglesworth, E., Gettelman, A., Conley, A., & Bailey, D. (2012). The influence of local feedbacks and northward heat transport on the equilibrium arctic climate response to increased greenhouse gas forcing. *Journal of Climate*, *25*(16), 5433-5450. Retrieved from https://doi.org/10.1175/JCLI-D-11-00622.1 doi: 10.1175/JCLI-D-11-00622.1

Marshal, J., & Plumb, R. A. (2008). *Atmosphere, ocean, and climate dynamics an introductory text* (first ed.). 30 Corporate Drive, Suite 400, Burlington, MA 01803 USA: Elsevier Academic Press.

Messori, G., Woods, C., & Caballero, R. (2018). On the drivers of wintertime temperature extremes in the high arctic. *Journal of Climate*, *31*(4), 1597-1618. Retrieved from https://doi.org/10.1175/JCLI-D-17-0386.1 doi: 10.1175/JCLI-D-17-0386.1

Peixoto, J. P., & Oort, A. H. (1992). *Physics of climate* (first ed.). 335 E. 45th Street New youer, NY 10017-3483: American Institue of Physics.

Pithan, F., & Mauritsen, T. (2014, Feb 02). Arctic amplification dominated by temperature feedbacks in contemporary climate models. *Nature Geoscience*, *7*, 181 EP -. Retrieved from https://doi.org/10.1038/ngeo2071

Sauer, T. (2012). *Numerical analysis* (second ed.). Pearson.

Smith, J. O. (2007). *Mathematics of the discrete fourier transform (dft)*. http://ccrma.stanford.edu/~jos/mdft/. (online book, 2007 edition. Accessed 1.9.2018)

Trenberth, K. E., & Caron, J. M. (2001). Estimates of meridional atmosphere and ocean heat transports. *Journal of Climate*, *14*(16), 3433-3443. Retrieved from https://doi.org/10.1175/1520-0442(2001)014<3433:EOMAAO>2.0.CO;2 doi: 10.1175/1520-0442(2001)014<3433:EOMAAO>2.0.CO;2

Vallis, G. K. (2017). *Atmospheric and oceanic fluid dynamics: Fundamentals and large-scale circulation* (second ed.). University Printing House, Cambridge CB2 2BS, United Kingdom: Cambridge University Press.

Warm and cold advection generated by short waves at mid levels. (2007). http://apollo.lsc.vsc.edu/classes/met130/

notes/chapter12/cold_warm_air_advection.html. (Accessed on 10.12.2018)